JGR Atmospheres

RESEARCH ARTICLE
10.1029/2019JD032275

# Favorable Circulation Patterns and Moisture Sources for Wintertime Extreme Precipitation Events Over the Balkhash-Junggar Region

**Xinsheng He[1], Wenyu Huang[1], Zifan Yang[1], Jonathon S. Wright[1], Bin Wang[2], Zuowei Xie[3], Tianpei Qiu[1], Wenhao Dong[4,5], Hui Lu[1], Xiang Li[6], and Jie Liao[7]**

[1]Ministry of Education Key Laboratory for Earth System Modeling, Department of Earth System Science (DESS), Tsinghua University, Beijing, China, [2]State Key Laboratory of Numerical Modeling for Atmospheric Sciences and Geophysical Fluid Dynamics (LASG), Institute of Atmospheric Physics (IAP), Chinese Academy of Sciences, Beijing, China, [3]International Center for Climate and Environment Sciences, Institute of Atmospheric Physics (IAP), Chinese Academy of Sciences, Beijing, China, [4]Cooperative Programs for the Advancement of Earth System Science, University Corporation for Atmospheric Research, Boulder, CO, USA, [5]Geophysical Fluid Dynamics Laboratory, NOAA, Princeton, NJ, USA, [6]National Marine Environmental Forecasting Center, Key Laboratory of Marine Hazards Forecasting, Ministry of Natural Resources, Beijing, China, [7]National Meteorological Information Center, Beijing, China

**Abstract** The Balkhash-Junggar (B-J) region is a typical dryland region with strong sensitivity to climate change. The snowstorms of the year 2009 caused financial damage worth of 2,516 million RMB. This study examines the dynamical features and the moisture sources associated with wintertime extreme precipitation over the B-J region. The analyses are based primarily on the data set from ERA-Interim during DJF 1979–2017. Both Lagrangian and Eulerian approaches are used to examine the moisture sources. An upper-tropospheric Rossby wave train that extends from the North Atlantic Ocean to the B-J region is found to play a leading role in the formation of 127 wintertime extreme precipitation events in the B-J region. This Rossby wave train deepens a cyclonic anomaly in the lower troposphere over the B-J region, which favors the development of strong southwesterly moisture transport and strong updrafts there. These conditions are favorable for the occurrence of extreme precipitation events over the B-J region. Lagrangian moisture source analysis indicates that most of the moisture for precipitation during these events comes from terrestrial sources, with central Asia the key moisture source region. The Eulerian moisture budget analysis further shows that most of the moisture for extreme precipitation enters the B-J region through its western boundary via enhanced southwesterly flow. These dynamical and moisture source analyses establish a set of valuable precursor conditions for predicting wintertime extreme precipitation events over the B-J region.

**Key Points:**
- A Rossby wave train extending from North Atlantic to Balkhash-Junggar region plays a leading role in triggering extreme precipitation events
- Moisture sources in central Asia provide nearly half of all moisture for the extreme precipitation events
- The majority (60.1%) of moisture contributions come from moisture uptake that occurs within 1–4 days before extreme precipitation events

**Supporting Information:**
- Supporting Information S1

**Correspondence to:**
W. Huang,
huangwenyu@mail.tsinghua.edu.cn

**Citation:**
He, X., Huang, W., Yang, Z., Wright, J. S., Wang, B., Xie, Z., et al. (2020). Favorable circulation patterns and moisture sources for wintertime extreme precipitation events over the Balkhash-Junggar region. *Journal of Geophysical Research: Atmospheres*, *125*, e2019JD032275. https://doi.org/10.1029/2019JD032275

Received 21 DEC 2019
Accepted 13 JUL 2020
Accepted article online 29 JUL 2020



## 1. Introduction

Drylands, commonly defined as regions with annual precipitation to potential evapotranspiration ratios less than 0.65, cover nearly 41% of the global land surface and are home to more than 38% of the global human population (Feng & Fu, 2013; Huang et al., 2017; Mike, 1996; Reynolds et al., 2007). According to observations and projections from climate models, global drylands have expanded dramatically over the past few decades, and this expansion is likely to continue in the near future (Feng & Fu, 2013; Guan et al., 2015; J. Huang, Ji, et al., 2016; J. Huang, Yu, et al., 2016; J. Huang et al., 2017; Ji et al., 2015). There are two possible causes for this expansion: One is a decreasing trend of precipitation over drylands and their adjoining regions (A. Dai, 2011, 2012; Dai & Zhao, 2017; Huang et al., 2016), while the other is increases in potential evapotranspiration due to rising temperatures associated with anthropogenic climate change (Huang et al., 2017; Scheff & Frierson, 2014; Sherwood & Fu, 2014; Zhao & Dai, 2015). Despite the global trend toward dryland expansion, some regions, such as the Junggar Basin, are experiencing dryland retreat. Precipitation increases and wetting trends have emerged in these regions over recent decades (Q. Li et al., 2011; Peng & Zhou, 2017; Shi et al., 2007; Wang et al., 2013), gradually transforming arid conditions into semiarid conditions (J. Huang, Ji, et al., 2016; Y. Li et al., 2015). To better understand the dynamics behind these changes, we must study the variations and formation mechanisms of precipitation over drylands.

The Balkhash-Junggar (B-J) region (43°N–52°N, 73°E–90°E; red box in Figure 1) is a typical dryland region containing Lake Balkhash and the Junggar Basin. According to a drought classification system based on the

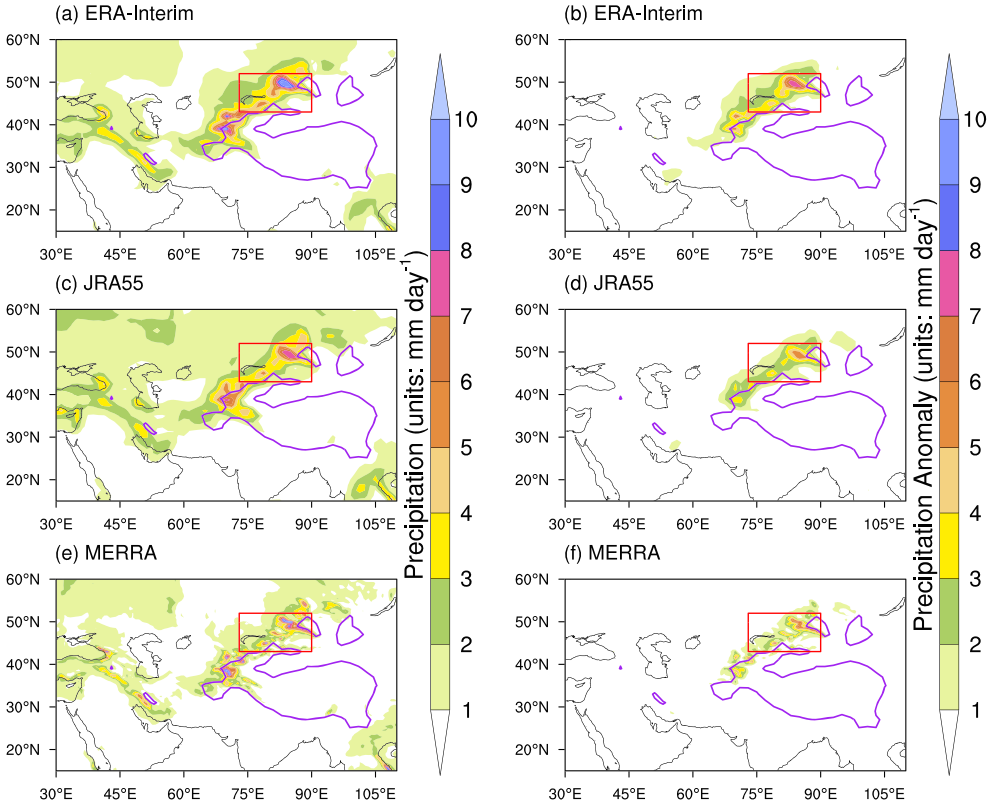


**Figure 1.** Horizontal distributions of composite-mean precipitation (left column; shading; units: mm day$^{-1}$) and precipitation anomalies (right column; shading; units: mm day$^{-1}$) over the Balkhash-Junggar (B-J) region and surrounding areas during all wintertime extreme precipitation events based on (a, b) ERA-Interim (DJF 1979–2017; 127 events), (c, d) JRA55 (DJF 1979–2017; 127 events), and (e, f) MERRA (DJF 1979–2015; 121 events). The B-J region as defined in this work is bounded by the red box. Regions bounded by solid purple lines have surface altitudes higher than 2,000 m.

standardized precipitation index (Ionita et al., 2016; McKee et al., 1993, 1995), more than 70% of winter months in the B-J region during 1979–2017 met the criteria for drought (supporting information Table S1). Owing to the location of the B-J region with abundant topographic features, precipitation in this region has relatively unique characteristics. The B-J region is located in the central part of the Eurasian continent, far from oceanic moisture sources. Further, the high-altitude Tianshan Mountains and the Tibetan Plateau (TP) are located to the south of the B-J region. These geographical barriers impede moisture import into the B-J region from evaporative sources over the Indian Ocean (Wang et al., 2017). As a consequence, the second largest desert in China, the Gurbantunggut, is located in the central Junggar Basin. The long-term average annual precipitation over northern Xinjiang (in the eastern B-J region) is less than 200 mm, which is relatively scarce (Y. Chen et al., 2014; B. Li et al., 2012; Q. Li et al., 2011; Peng & Zhou, 2017; Qian et al., 2001; Q. Zhang et al., 2012; C. Zhao et al., 2015). By contrast, the annual precipitation is much larger over the Ili River Valley, in the southern B-J region, where cumulative annual precipitation ranges from 300 to 530 mm (H. Wang et al., 2013). The greater precipitation over the Ili River Valley (southern B-J region) relative to other parts of the B-J region is particularly pronounced during winter (DJF), when cumulative precipitation amounts in the Ili River Valley range from 24 to 60 mm (H. Wang et al., 2013).

There are two primary sources for water resources in the B-J region: precipitation and meltwater from glaciers and snow cover. In particular, the Tianshan mountains (south of the B-J region) contain approximately 9,035 glaciers covering an area of 9,225 km$^2$, with an estimated ice storage capacity of 1,011 km$^3$ (Shi et al., 2009). About 20% of annual runoff in the B-J region comes from the melting of glaciers and winter snow (Cao et al., 2018). However, the ultimate source of almost all water mass in glaciers and snow cover

remains precipitation. The wintertime precipitation, typically in the form of snow, plays a critical role in the formation and maintenance of glaciers and snow cover in the B-J region and its surrounding areas.

Some of the annual precipitation over the B-J region arrives in the form of extreme snowfall events, which may in turn lead to severe snow disasters. For example, a series of snowstorms hit the B-J region between 22 December 2009 and 28 February 2010. Cumulative precipitation over this period exceeded 50 mm over most of the B-J region and reached 940 mm in Altay. This series of extreme snowstorms affected more than 3.14 million people and was linked to 33 deaths, with estimated economic losses of 2,516 million RMB (R. Li et al., 2015; J. Zhang et al., 2013; S. Zhang & Zhu, 2011). The extent of these damages highlights the need to examine the formation mechanisms responsible for the occurrence of wintertime extreme precipitation in the B-J region.

The characteristic timescale of wintertime extreme precipitation events falls within the synoptic timescale of several hours to several days. It is therefore natural to study the mechanisms behind wintertime extreme precipitation over the B-J region on the synoptic timescale. Several studies have examined the circulation patterns responsible for the formation of specific wintertime extreme precipitation events over the B-J region on a case-by-case basis. Most of these studies revealed that a necessary condition for wintertime extreme precipitation over the B-J region is a coupling between lower-tropospheric convergence and middle/upper-tropospheric divergence (An & Zhao, 2013; Li et al., 2014; Liu et al., 2011). This coupling is also among the necessary dynamic conditions for most precipitation around the world. However, these individual case studies drew rather different conclusions about the large-scale circulation patterns that favor the occurrence of wintertime extreme precipitation in the B-J region. Liu et al. (2011) suggested that coupling between a shortwave trough separated from a preexisting cutoff low and a persistent blocking high over the Ural Mountains and western Siberia led to an extreme precipitation event over the northern B-J region during 4–7 January 2010. An and Zhao (2013) implicated coupling between a shortwave trough around the B-J region and the India-Burma trough as contributing to an extreme precipitation event during 22–23 February 2010. Finally, Y. Li et al. (2014) found that the eastward migration of a cyclonic anomaly originating from central Asia led to an extreme snowfall event during 21–23 February 2012 over the B-J region. Based on these disparate conclusions, a question naturally arises: Can we identify any circulation patterns that are often favorable to the development of wintertime extreme precipitation events over the B-J region? The differences in the circulation patterns documented by these previous studies may be related to case-to-case variability, perhaps compounded by intrinsic dependence on the climate state. Therefore, to answer the above question, we must first examine a large number of wintertime extreme precipitation events over the B-J region under a wide range of climate states.

In addition to a favorable circulation pattern, an abundant supply of moisture is also necessary for the occurrence of extreme precipitation (Trenberth, 1999, 2011). There are two common methodologies for diagnosing the sources of moisture for precipitation: Lagrangian moisture attribution analysis and Eulerian moisture budget analysis. In Lagrangian moisture attribution analysis (Drumond, Nieto, & Gimeno, 2011; Drumond, Nieto, Hernnández, & Gimeno, 2011; Durán-Quesada et al., 2010; Salih et al., 2015; Stohl & James, 2004, 2005; Stohl et al., 2008; Sun & Wang, 2014), precipitation from an air parcel is decomposed according to moisture uptake (or loss) by the parcel from (or to) its environment along trajectories integrated backward in time. In Eulerian moisture budget analysis (Howland & Sikdar, 1983; Jin & Zangvil, 2009; Kim et al., 2019; Simmonds et al., 1999; Tiwari et al., 2017), precipitation is viewed as the sum of local evapotranspiration, the (negative) local tendency of precipitable water, and large-scale moisture convergence. Dai et al. (2007) used an Eulerian methodology to analyze the moisture supply for precipitation over the Xinjiang region (within the B-J region) during 1980–2000. They found that the moisture for the precipitation during winter, spring, and autumn entered the region mainly through the western boundary, while that during summer came mainly from the north or northwest. The Lagrangian method is able to construct a source-receptor relationship (Chen et al., 2012; Gimeno et al., 2010, 2012; Stohl & James, 2004, 2005, Stohl et al., 2008; Sun & Wang, 2014; Vazquez et al., 2016; Winschall et al., 2014) and is therefore typically superior to the Eulerian method with respect to identifying the locations and quantitative contributions of different moisture source regions. Until now, the Lagrangian method has only been applied to summertime precipitation over the B-J region and its surrounding areas (Hua, Zhong, & Ma, 2017; Huang, Chang, et al., 2017; Wang et al., 2017; Yao et al., 2018). It would be quite valuable to determine the moisture sources for

wintertime extreme precipitation events in the B-J region using Lagrangian moisture attribution analysis. The B-J region and its surrounding continental areas are colder and drier during winter than during other seasons. Local evapotranspiration within the B-J region is thus much weaker during winter than during other seasons. Consequently, another question arises: Where are the key moisture source regions for extreme precipitation events over the B-J region?

In this paper, we examine the formation mechanisms of the wintertime extreme precipitation events by identifying the favorable circulation patterns and key moisture source regions from a synoptic perspective. The paper is organized as follows. In section 2, we introduce the data, an algorithm for defining the wintertime extreme precipitation events over the B-J region, the calculation of the wave activity flux, and the methods for heat budget analysis, Lagrangian moisture source attribution, and Eulerian moisture budget analysis. In section 3, we present the basic characteristics of the wintertime extreme precipitation events over the B-J region. In section 4, we identify the favorable circulation patterns for wintertime extreme precipitation events over the B-J region by constructing the composite evolution of the circulation patterns and wave activity fluxes around the time of onset of these events. In addition, we analyze composite variations in lower-troposphere temperature prior to the onset of extreme precipitation events. In section 5, we examine the moisture sources for extreme precipitation events over the B-J region using both Lagrangian and Eulerian approaches. We close the paper with summary and concluding remarks in section 6.

## 2. Data and Methods

### 2.1. Data

This study focuses on extreme precipitation events over the B-J region (43°N–52°N, 73°E–90°E) during winter months from December 1979 to February 2018. The winter months of a given year refer to December of that year and January and February of the following year (DJF), so that the study period is referred to as DJF 1979–2017. Diagnostic analyses are based primarily on the European Centre for Medium-Range Weather Forecasts (ECMWF) Interim Re-Analysis (ERA-Interim; Dee et al., 2011) during DJF 1979–2017. ERA-Interim products used include 6-hourly pressure-level analyses of geopotential height, temperature, specific humidity, horizontal winds, and vertical velocity, 6-hourly analyses of surface air temperature at 2-m height, total column water vapor, vertical integral of horizontal water vapor flux, 12-hourly cumulative estimates of total precipitation and surface evaporation, and monthly means of total precipitation. All variables are provided on a $1° \times 1°$ latitude-longitude grid. We also compare ERA-Interim precipitation to precipitation estimates from the Japanese 55-year Reanalysis (JRA-55; Kobayashi et al., 2015) and the Modern-Era Retrospective-analysis for Research and Applications (MERRA; Rienecker et al., 2011). The JRA-55 precipitation is provided 3-hourly on a $1.25° \times 1.25°$ latitude-longitude grid. The MERRA precipitation is based on daily averages on a $0.5° \times 0.67°$ latitude-longitude grid.

Backward trajectories of air parcels initiated over the B-J region are calculated using version 2.0 of the LAGRangian ANalysis TOol (LAGRANTO; Sprenger & Wernli, 2015; Wernli & Davies, 1997). These trajectories are then used to determine the moisture source distributions for precipitation over the B-J region. To drive the LAGRANTO model, we use 6-hourly horizontal winds, vertical velocity, temperature, and specific humidity on 60 model $\eta$ levels together with 6-hourly surface pressure. All variables are from ERA-Interim on a $1° \times 1°$ latitude-longitude grid. We keep the original temporal resolutions of the variables when conducting the Lagrangian moisture attribution analysis but use daily averages when conducting all other diagnostic analyses.

### 2.2. Definition of Wintertime Extreme Precipitation Events

Wintertime extreme precipitation days are identified as those days with daily precipitation in the B-J region exceeding the 95th percentile (2.22 mm day$^{-1}$) during DJF 1979–2017. The 95th percentile is adopted following Peterson et al. (2008) and Zhang et al. (2011), who used this threshold to study extreme precipitation over North America and global land areas, respectively. An extreme event is defined as a period that includes one or more consecutive extreme precipitation days. We also allow for one nonextreme precipitation day between any two extreme precipitation days in defining extreme events. Based on this definition, we obtain 127 extreme precipitation events comprising a total of 191 wintertime days, of which 177 were extreme precipitation days.

### 2.3. Calculation of the Wave Activity Flux

We calculate the wave activity fluxes using the formulation developed by Takaya and Nakamura (2001). The horizontal formulation of wave activity flux can be formulated as

$$\mathbf{W_{2d}} = \frac{p}{p_0}\frac{\cos\phi}{2|U|}\begin{pmatrix} \frac{u}{a^2\cos^2\phi}\left[\left(\frac{\partial\psi'}{\partial\lambda}\right)^2 - \psi'\frac{\partial^2\psi'}{\partial\lambda^2}\right] + \frac{v}{a^2\cos\phi}\left[\frac{\partial\psi'}{\partial\lambda}\frac{\partial\psi'}{\partial\phi} - \psi'\frac{\partial^2\psi'}{\partial\lambda\partial\phi}\right] \\ \frac{u}{a^2\cos\phi}\left[\frac{\partial\psi'}{\partial\lambda}\frac{\partial\psi'}{\partial\phi} - \psi'\frac{\partial^2\psi'}{\partial\lambda\partial\phi}\right] + \frac{v}{a^2}\left[\left(\frac{\partial\psi'}{\partial\phi}\right)^2 - \psi'\frac{\partial^2\psi'}{\partial\phi^2}\right] \end{pmatrix}, \quad (1)$$

where $(\phi, \lambda)$ are the latitude and longitude of the location, $(u, v)$ are the climatological mean horizontal winds, $|U| = \sqrt{u^2 + v^2}$ is the magnitude of horizontal winds, $p$ is pressure, $\psi$ is the geostrophic stream function, $\psi'$ is the deviation of $\psi$ relative to the climatological mean ($\psi' = \frac{gz'}{f}$), $g$ is the gravitational acceleration, $z'$ is the low-pass-filtered geopotential height anomalies, and $f$ is the Coriolis parameter. The constants $p_0$ and $a$ represent the reference pressure ($p_0 = 1{,}000$ hPa) and the radius of the Earth ($a = 6{,}371$ km), respectively.

### 2.4. Method for Heat Budget Analysis

The thermodynamic energy equation can be formulated as (e.g., Peixoto & Oort, 1992)

$$\frac{\partial T}{\partial t} = -\mathbf{v}\cdot\nabla T - \omega\frac{\partial T}{\partial p} + \omega\frac{R}{c_p}\frac{T}{p} + \frac{Q}{c_p}, \quad (2)$$

where $t$ and $p$ are time and pressure coordinates, $\mathbf{v}$ is the horizontal wind vector, $\omega$ is the vertical pressure velocity $\left(\frac{dp}{dt}\right)$, $T$ is temperature, $Q$ is diabatic heating, $R$ is the specific gas constant, and $c_p$ is the specific heat capacity. The left-hand side of Equation 2 is the local temperature tendency $\left(\frac{\partial T}{\partial t}\right)$, while the four terms on the right-hand side (from left to right) represent horizontal temperature advection, vertical temperature advection, adiabatic heating due to compression or expansion, and diabatic heating. All terms in Equation 2 are calculated except the diabatic heating term, which is estimated as the residual (Ling & Zhang, 2013; Ling et al., 2013; Zhang & Ling, 2012).

### 2.5. Method for Lagrangian Evaporative Moisture Source Analysis

The Lagrangian approach we use to identify and estimate the sources of evaporative moisture for extreme precipitation events over the B-J region contains two steps. The first step is to calculate backward trajectories. The second step is to catalog evaporative contributions along those trajectories to identify and quantify the sources of moisture for extreme precipitation.

#### 2.5.1. Calculating Backward Trajectories

We use version 2.0 of the LAGRANTO, developed by Sprenger and Wernli (2015), to calculate backward Lagrangian trajectories for all air parcels located over the B-J region during extreme precipitation events. Here, the B-J region is defined as the three-dimensional volume bounded by (43°N–52°N, 73°E–90°E, and 1,000 to 480 hPa). The upper limit (480 hPa) used here is the same as that used by Sodemann et al. (2008). Specific humidity decreases with height and is consistently smaller than 0.3 g kg$^{-1}$ above 480 hPa over the B-J region during winter (Figure S1). Air parcels above this altitude therefore contribute little to the moisture budget overall. Moreover, we focus mainly on evaporative sources, which are best characterized by humidity changes within the boundary layer (BL). The isobaric surface at 480 hPa is well above the BL in the B-J region, so that this upper limit has negligible impact on our ability to capture evaporative sources. Trajectory starting points are defined to be horizontally and vertically equidistant from each other, with a horizontal spacing of 100 km and a vertical spacing of 40 hPa. For each of the 191 days associated with the 127 extreme events, air parcel trajectories are initiated four times per day (00:00, 06:00, 12:00, and 18:00 UTC) and integrated 240 hr (10 days) backward in time. The 10-day calculation time for backward trajectories is chosen to be slightly longer than the average residence time for atmospheric moisture (~8 days;

Trenberth, 1998, 1999). The evolutions of specific humidity and relative humidity (RH) are recorded along each backward trajectory at regular time intervals spaced 6 hr apart (with a total length of 240 hr).

#### 2.5.2. Attributing Evaporative Moisture Sources

Evaporative moisture sources are attributed using information recorded along the backward trajectories. The moisture source attribution method is based on the assumption that moisture increases along a trajectory correspond to net moisture sources, while moisture decreases correspond to net moisture sinks (James et al., 2004; Stohl & James, 2004). In practice, we adopt the moisture attribution algorithm developed by Sodemann et al. (2008), which includes the following three substeps.

First, we estimate the precipitation over the B-J region based on moisture variations along the backward trajectories during the period from $t = -6$ hr to $t = 0$ hr. The estimated precipitation below any atmospheric column within the B-J region is calculated as

$$P_{\mathrm{LAG}} = -\frac{\Delta p}{\rho_w g}\sum_{k=1}^{k=k_{\mathrm{top}}} \Delta q_k^0, \tag{3}$$

where $P_{\mathrm{LAG}}$ is the estimated precipitation produced in the column based on the Lagrangian trajectories, $\rho_w$ is the density of water, $g$ is the gravitational acceleration, $k$ is the vertical index of the air parcels ($1 \le k \le k_{\mathrm{top}}$; $k_{\mathrm{top}} = 14$) over this position, $\Delta p$ is the vertical depth of an air parcel ($\Delta p = 40$ hPa), and $\Delta q_k^0$ is the moisture decrease recorded for the $k$th air parcel ($\Delta q_k^t = q_k^t - q_k^{t-6\ \mathrm{hr}}$ for $t = 0$ hr). In practice, only air parcels with moisture decreases ($\Delta q_k^0 < 0$) and RH exceeding a threshold value of 70% are used to estimate precipitation.

Second, we identify and discount potential moisture sources. For each air parcel initiated over the B-J region, locations along its backward trajectory with moisture increases (i.e., $\Delta q_k^t > 0$ for $-234\ \mathrm{hr} \le t \le -6$ hr) are considered as potential moisture sources. However, moisture gains identified for previous time steps may be partially released as precipitation before the air parcels reach the B-J region. To account for this possibility, an adjustment algorithm is applied to all identified potential moisture sources. In this algorithm, the adjusted moisture uptake $\Delta' q_k^i$ at time step $i$ is calculated as

$$\Delta' q_k^i = \Delta q_k^i \times \left(1 + \frac{\Delta q_k^j}{q_k^{j-6\ \mathrm{hr}}}\right). \tag{4}$$

Here, $j$ denotes a time step when precipitation occurred ($\Delta q_k^j < 0$, $j < 0$ and $|\Delta q_k^j| < q_k^{j-6\ \mathrm{hr}}$) prior to the air parcel reaching its initiation point over the B-J region, $i$ denotes a time step prior to $j$ with moisture uptake ($\Delta q_k^i > 0$; $i < j < 0$), and $q_k^{j-6\ \mathrm{hr}}$ is the specific humidity of the air parcel at time step $j - 6$ hr (i.e., 6 hr before the precipitation at time step $j$). The adjusted moisture uptake $\Delta' q_k^i$ is therefore modified from its original value by multiplying a coefficient between 0 and 1 that depends on the relative moisture loss during precipitation. A larger loss corresponds to a smaller coefficient. This type of adjustment algorithm can be referred to as a "discounting algorithm" and the adjusted moisture uptake as "discounted moisture uptake."

Third, we quantify evaporative moisture sources using only moisture gains that occur within the BL, as only moisture sources within the BL can be viewed as evaporative sources (Sodemann et al., 2008). To judge whether an air parcel is located within the BL, we apply the equation

$$\mathrm{BLH} + H_0 \ge 8,000 \times \ln\left(\frac{1,014}{p}\right), \tag{5}$$

where $p$ is the pressure of the air parcel (units: hPa), BLH is the local BL height from ERA-Interim (units: m), and $H_0$ is the altitude of the surface (units: m).

### 2.6. Method for Eulerian Moisture Budget Analysis

Following Trenberth and Guillemot (1995), we write the Eulerian moisture budget equation as

$$P = -\frac{\partial w}{\partial t} - \nabla \cdot \frac{1}{g}\int_{p_s}^{p_t} q\mathbf{v}dp + E, \tag{6}$$

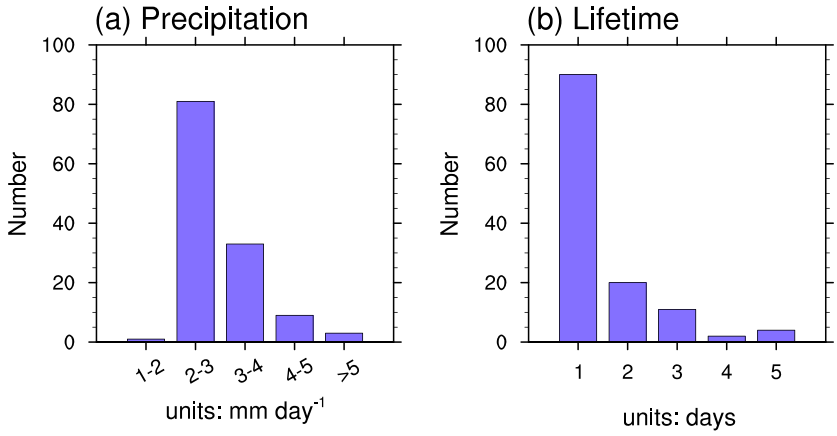


**Figure 2.** Frequency distributions of (a) area-averaged precipitation intensity (units: mm day$^{-1}$) and (b) event lifetime (units: days) among the 127 extreme precipitation events that occurred over the Balkhash-Junggar (B-J) region during DJF 1979–2017.

where $P$ is precipitation, $w$ is precipitable water, $t$ is time, $g$ is the gravitational acceleration, $q$ is specific humidity, $\mathbf{v}$ is the horizontal wind vector, $E$ is evapotranspiration (or evaporation), $p$ is pressure, and $p_s$ and $p_t$ are the pressures at the surface and model top, respectively. The precipitable water, $w$, is defined as the mass-weighted vertical integral of specific humidity $q$ through the tropospheric column (i.e., $w = \frac{1}{g}\int_{p_s}^{p_t} q dp$). The precipitation $P$ over a given region is therefore modulated by the temporal fluctuations in precipitable water $\left(-\frac{\partial w}{\partial t}\right)$, large-scale moisture convergence $\left(-\nabla, \cdot \frac{1}{g}\int_{p_s}^{p_t}, q, \mathbf{v}, d, p\right)$, and surface evapotranspiration or evaporation ($E$) that occur within that region. In practice, large-scale moisture convergence into the B-J region is calculated as the sum of the moisture fluxes across the four lateral boundaries of the region.

## 3. Basic Characteristics of the Extreme Precipitation Events

Figures 1a and 1b present the composite-mean (averaged in days) horizontal distribution of ERA-Interim precipitation and precipitation anomalies over the B-J region during the 127 extreme events. The spatial pattern of precipitation is oriented along a southwest-northeast axis, consistent with the orientation of the mountains that extend from the northwestern TP to the Altai Mountains. The barrier effect of these mountains evidently plays a central role in shaping the horizontal distribution of wintertime extreme precipitation within the B-J region. The precipitation maximum, which exceeds 10 mm day$^{-1}$, is located in the northeastern portion of the B-J region, west of the Altai mountains. There are also several localized precipitation maxima with values just over 10 mm day$^{-1}$ located along the northwestern edge of the TP. Meanwhile, evident positive precipitation anomalies are present over most of the B-J region with a maximum larger than 7 mm day$^{-1}$ (Figure 1b). The locations of localized maxima for precipitation anomaly are the same as those for precipitation. Both of the precipitation and its anomaly suggest that the formation mechanisms for extreme precipitation over the B-J region may share similarities with those for extreme precipitation over the northwestern TP. We find the same characteristics in two other reanalysis data sets (JRA-55 and MERRA; Figures 1c–1f), including the orientation of the precipitation band, the geographical position of the maximum precipitation, and the concurrence with intense precipitation over the northwestern TP. We therefore use ERA-Interim alone to examine the formation mechanisms for wintertime extreme precipitation events over the B-J region.

Area-mean precipitation amounts over the B-J region during the extreme precipitation events ranged from 1.8 to 5.6 mm day$^{-1}$. Among the identified extreme precipitation events, 81 events (63.8% of the total) had precipitation rates ranging from 2 to 3 mm day$^{-1}$, 33 events (26.0%) had precipitation rates ranging from 3 to 4 mm day$^{-1}$, 9 events (7.1%) had precipitation rates ranging from 4 to 5 mm day$^{-1}$, and 3 events (2.4%)

had precipitation rates exceeding 5 mm day$^{-1}$ (Figure 2a). Only one event had a mean precipitation rate less than 2 mm day$^{-1}$ (0.8% of the total). The existence of extreme events with precipitation rates less than the 2.2 mm day$^{-1}$ threshold for defining extreme precipitation days is due to our allowance of nonextreme precipitation days within extreme events, as described above. Figure 2b shows the frequency distribution of event lifetimes among the 127 extreme precipitation events. The lifetimes of extreme precipitation events ranged from 1 to 5 days, with the majority (90 events; 70.9%) having lifetimes of 1 day. Among the events that lasted longer than 1 day, 20 events (15.7%) had lifetimes of 2 days, 11 events (8.7%) had lifetimes of 3 days, and 6 events (4.7%) had lifetimes ranging from 4 to 5 days.

## 4. Favorable Circulation Patterns

In this section, we identify and describe the circulation patterns that favor the formation of wintertime extreme precipitation events over the B-J region.

### 4.1. Evolution of Upper-Tropospheric Circulation Anomalies

Figure 3 shows the evolution of geopotential height anomalies and wave activity fluxes on the 300 hPa isobaric surface from Day −12 to Day +4 at 2-day intervals composited on the 127 extreme precipitation events. A more detailed evolution at daily intervals is provided in Figure S2. Here, Day 0 refers to the first day (i.e., the onset) of the extreme event, and anomalies are calculated relative to the climatological mean during 1979–2017. The analysis begins at Day −12 because significant cyclonic and anticyclonic anomalies that may serve as precursor signals for the occurrence of extreme precipitation events emerge around this time. The analysis ends at Day +4 because the maximum duration among all identified events is 5 days (Day 0 to Day +4). The wave activity fluxes are calculated using the formulation introduced in section 2.3. On Day 0 (Figure 3g), the circulation pattern around the B-J region is characterized by a northwest-southeast-oriented dipole structure with significant cyclonic and anticyclonic anomalies in the northwest and southeast sides of the B-J region, respectively. The magnitude of the cyclonic anomaly reaches −150 gpm, while that of the anticyclonic anomaly reaches 90 gpm. The B-J region is located at the boundary between the cyclonic and anticyclonic anomalies.

Figure 4 shows composite vertical cross sections of meridionally averaged geopotential height anomalies, vertical velocities, zonal wind anomalies, and temperature anomalies on Day 0 during the 127 extreme precipitation events. Here, meridional averages are calculated across the latitude band corresponding to the B-J region (43°N–52°N). At the onset of the extreme events (Day 0), the dipole structure around the B-J region is confined to the upper troposphere (Figure 4a). The cyclonic anomalies that dominate the middle and lower troposphere tilt westward with height, indicating baroclinic energy conversion from available potential energy to kinetic energy. As shown by Lin et al. (1991), positive energy conversion (from available potential energy to kinetic energy) in regions of strong winds and large-scale convergence in cyclonic anomalies tends to further intensify those anomalies. The cyclonic anomalies associated with wintertime extreme precipitation in the B-J region favor ascending motion extending upward through almost the entire troposphere (Figure 4b), which helps to trigger the onset of extreme precipitation. The composite mean also features a remarkable intensification of the westerly winds in the upper troposphere (Figure 4c) and the formation of a temperature front in the lower troposphere above the B-J region (Figure 4d) with a pronounced warm anomaly upward to the upper troposphere to the east of the B-J region. A detailed heat budget analysis for the temperature variations in the lower troposphere is provided in section 4.2. This warm anomaly together with cyclonic anomaly (Figure 4a) creates an evident poleward heat flux in the lower troposphere (Figure S3), suggesting a positive baroclinic energy conversion (Dole & Black, 1990).

We further analyze the evolution of geopotential height anomalies and wave activity fluxes on the 300 hPa isobaric surface to identify any robust precursor signals for the dipole structure over the B-J region on Day 0. The cyclonic anomaly within this dipole structure can be traced back to a cyclonic anomaly located near the coastline of the Barents Sea (around 45°E) on Day −12, while the anticyclonic anomaly can be traced back to an anticyclonic anomaly centered over the eastern Mediterranean Sea (38°N, 30°E; around the Middle East region) on Day −12 (Figure 3a). The precursor anticyclonic anomaly is situated to the southwest of the precursor cyclonic anomaly on Day −12, indicating that the northwest-southeast orientation of the dipole structure emerges later. Westerly winds around the precursor anticyclonic anomaly are much stronger than those around the precursor cyclonic anomaly (not shown), so that the precursor anticyclonic anomaly propagates

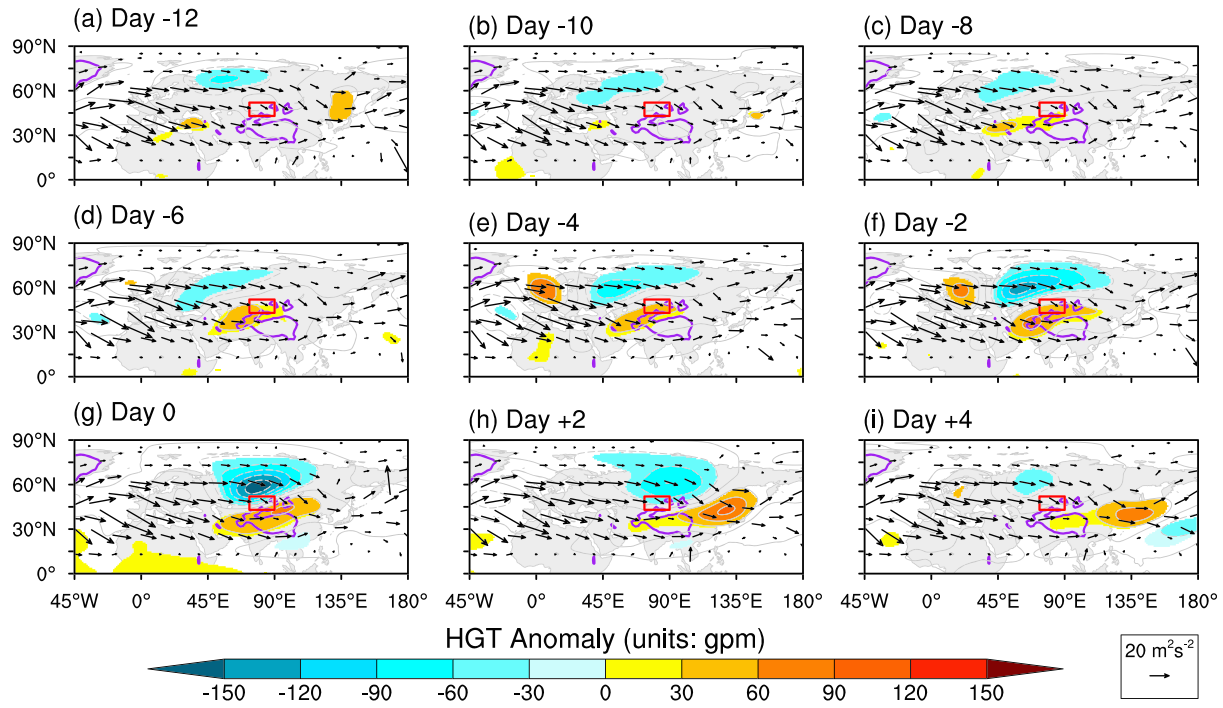


**Figure 3.** (a–i) Time evolution of composite geopotential height anomalies (contour and shading; units: gpm) and horizontal wave activity fluxes (vector; units: $m^2 s^{-2}$) on the 300 hPa isobaric surface between Day −12 and Day +4 at 2-day intervals around the 127 identified wintertime extreme precipitation events over the Balkhash-Junggar (B-J) region. Shading indicates that composite geopotential height anomalies are significant at 95% confidence level based on two-tailed Student's *t* tests. The B-J region is marked by the red box, and regions with surface altitudes higher than 2,000 m are bounded by solid purple lines.

eastward faster than the cyclonic anomaly. The anticyclonic anomaly gradually propagates along the TP during the period from Day −8 to Day −6. By Day −6, this anticyclonic anomaly is located southeast of the cyclonic anomaly, thus establishing the northwest-southeast orientation of the dipole structure (Figure 3d). Meanwhile, a pair of cyclonic and anticyclonic anomalies (Figure 3d; see also anomalies within green circles in Figure S4) that emerge over the North Atlantic Ocean combine with the two precursor anomalies to form a Rossby wave train on Day −6 (Figure 3d; see also the blue arrow in Figure S4). This Rossby wave train is most evident on Day −4 (Figure 3e). Continuous wave activity fluxes along this wave train strengthen the development of the two circulation anomalies that constitute the dipole structure. By Day 0, the cyclone-anticyclone pair that initially emerged over the North Atlantic Ocean has disappeared due to Rossby wave energy dispersion (Figure 3g), while the dipole structure has migrated into position over the B-J region. The dipole weakens quickly as the Rossby wave energy propagates downward (Figures 3h and 3i).

### 4.2. Evolution of Lower-Tropospheric Circulation and Temperature Anomalies

Figures 5a–5d show the evolution of composite geopotential height anomalies on the 850 hPa isobaric surface. Unlike in the upper troposphere, there is no northwest-southeast-oriented dipole structure in the lower-tropospheric circulation over the B-J region on Day 0 (Figure 5c). Instead, the B-J region is covered by the southern part of a significant cyclonic anomaly with its peak magnitude exceeding −75 gpm. The absence of an anticyclonic anomaly in the lower troposphere to the south or southeast of this cyclonic anomaly can be explained by the presence of the TP to the south and southeast of the B-J region. The average altitude of this part of the TP exceeds 4,000 m and therefore extends above the 850 hPa isobaric surface. Compared to the upper-tropospheric cyclonic anomaly (Figure 3g), the lower-tropospheric cyclonic anomaly is located further toward the southeast. This northwestward tilt with increasing height is also evident in the composite vertical cross section of geopotential height anomalies on Day 0 (Figure 4a).

A Rossby wave train is evident in the lower troposphere on Day −6 (Figure 5a; see also the blue arrow in Figure S5), extending from the North Atlantic Ocean to the northwestern edge of the B-J region. This Rossby wave train consists of three centers of action: the pair of cyclonic and anticyclonic anomalies over

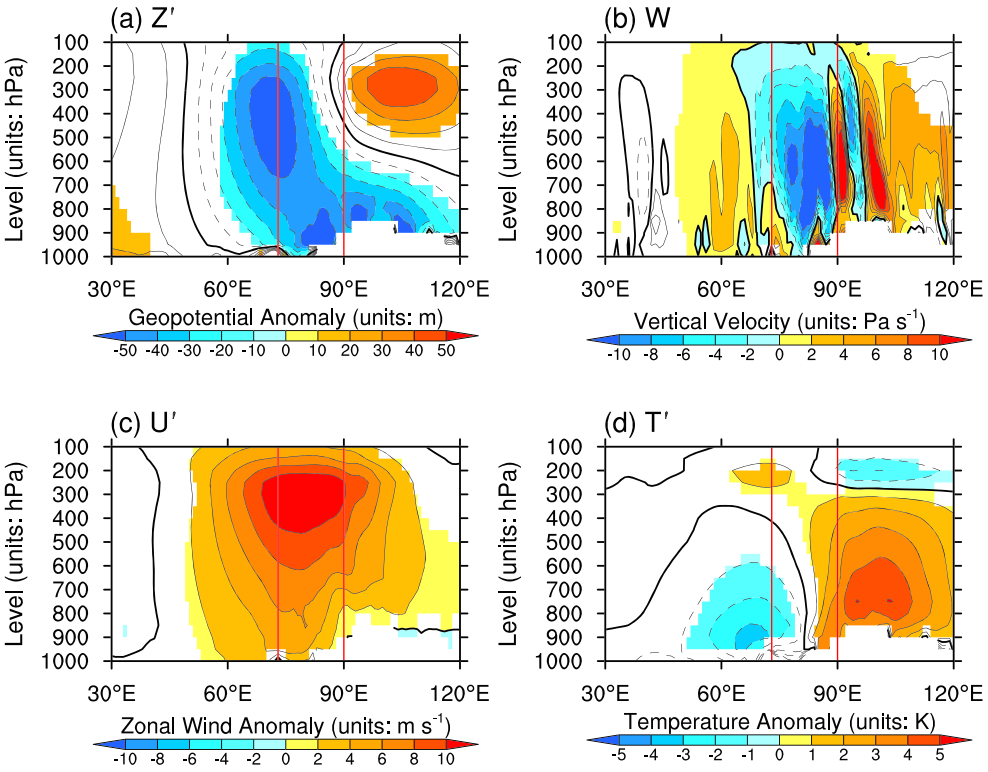


**Figure 4.** Composite vertical cross sections of meridionally averaged (a) geopotential height anomalies (contour and shading; units: gpm), (b) vertical velocity (contour and shading; units: Pa $s^{-1}$), (c) zonal wind anomalies (contour and shading; units: m $s^{-1}$), and (d) temperature anomalies (contour and shading; units: K) over the Balkhash-Junggar (B-J) region within 43°N–52°N on Day 0 of the 127 extreme precipitation events. Negative (positive) values are marked by dashed (solid) lines, while zero values are marked by heavy lines. Shading indicates that composite anomalies are significant at 95% confidence level based on two-tailed Student's *t* tests. The boundaries of the B-J region are marked by the two red lines.

the North Atlantic and the cyclonic anomaly northwest of the B-J region. Day −6 also corresponds to the time when a Rossby wave train consisting of four centers of action forms in the upper troposphere (Figure 3d; see also Figure S4). Except for the topographically truncated easternmost center in the lower troposphere, there is a one-to-one correspondence between the centers of action in the lower-tropospheric and upper-tropospheric Rossby wave trains, albeit with slight shifts in the geographical positions of the centers. The lower-tropospheric signal can thus be regarded as the near-surface manifestation of the upper-tropospheric Rossby wave train. The easternmost center of action in the lower-tropospheric Rossby wave train (the cyclonic anomaly northwest of the B-J region) intensifies and migrates eastward over 6 days immediately prior to onset (Day −6 to Day 0; Figures 5a–5c).

Figures 5e–5h show the evolution of composite temperature anomalies on the 850 hPa isobaric surface. On Day −6, significant cold anomalies of −1 K are found to the northwest of the lower-tropospheric cyclonic anomaly near the B-J region, with significant warm anomalies exceeding +2 K present to its southeast (Figure 5e). As the B-J region is located to the southeast of this anomaly, it is largely covered by warm temperature anomalies of ∼1 K. The temperature anomalies on the 850 hPa isobaric surface around the cyclonic anomaly thus appear as a temperature dipole, which can be partially explained by the antisymmetric structure of the horizontal wind anomalies associated with the cyclonic anomaly. To the northwest of the anomaly, northerly winds advect colder air southward. Conversely, southerly winds to the southeast of the anomaly advect warmer air northward. Owing to the eastward migration and intensification of the lower-tropospheric cyclonic anomaly, the temperature dipole also migrates eastwards and becomes stronger (Figures 5e–5g). As a consequence, lower-tropospheric temperatures over the B-J region drop sharply around the onset of wintertime extreme precipitation. Specifically, whereas temperature anomalies over

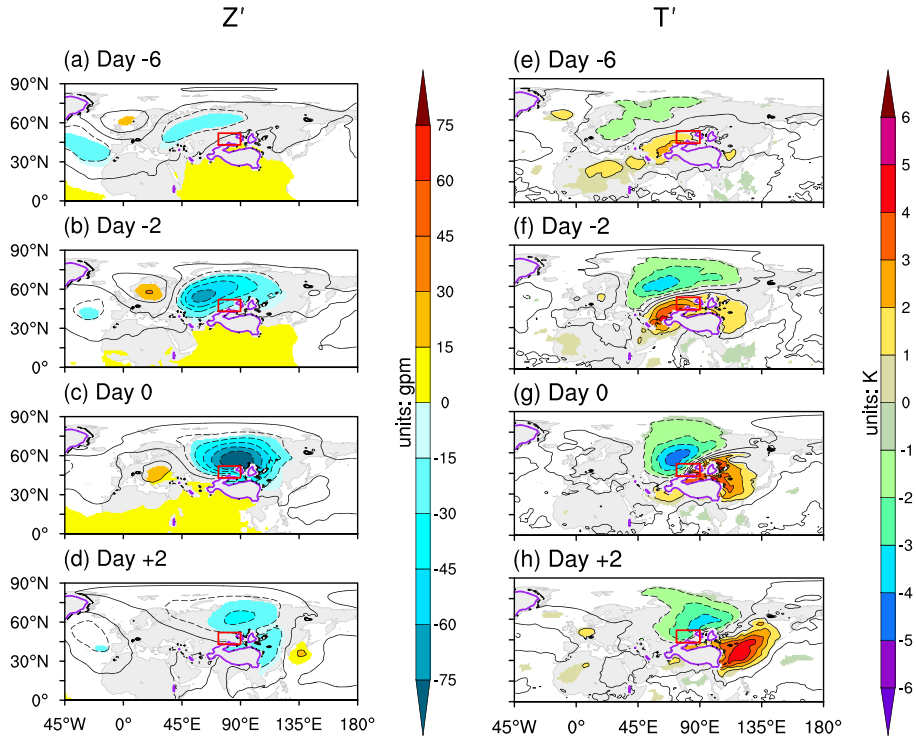


**Figure 5.** Evolution of composite geopotential height anomalies (panels a–d; contour and shading; units: gpm) and temperature anomalies (panels e–h; contour and shading; units: K) on the 850 hPa isobaric surface for Day −6 (top), Day −2 (second row), Day 0 (third row), and Day +2 (bottom) around the 127 wintertime extreme precipitation events over the Balkhash-Junggar (B-J) region. Negative anomalies are marked by dashed lines; nonnegative anomalies are marked by solid lines. Shading indicates that composite anomalies are significant at 95% confidence level based on two-tailed Student's *t* tests. The B-J region is marked by the red box, and regions with surface altitudes higher than 2,000 m are bounded by solid purple lines.

much of the B-J region are approximately +3 K on Day −2 (Figure 5f), significant negative anomalies set in on Day 0 and persist until Day +2 (Figures 5g and 5h).

In addition to horizontal temperature advection, processes such as vertical temperature advection, adiabatic heating, and diabatic heating can also cause temperature variations. Powerful updrafts that emerge around the onset of the extreme precipitation events (Figure 4b) suggest that both vertical temperature advection and adiabatic process may play significant roles in temperature variations above the B-J region around the onset of extreme precipitation events. To better quantify the contributions of each physical process to temperature variations over the B-J region, we conduct a heat budget analysis on the 850 hPa isobaric surface based on the approach as described in section 2.4.

The area-averaged temporal evolution of each term in the heat budget over the B-J region from Day −12 to Day +4 is shown in Figure 6, supplemented by the evolutions of anomalies in specific humidity, temperature, and geopotential height at selected levels in Figure 7. Conditions over the B-J region are largely unaffected by the lower-tropospheric cyclonic anomaly prior to Day −3 but respond significantly to this anomaly between Day −2 and Day +1 (Figure 6; solid lines in Figure 7). The primary influence on the lower troposphere over the B-J region during winter is the Siberian high, with average conditions characterized by weak downdrafts. At 850 hPa, these weak downdrafts result in an approximate three-way balance among heating due to adiabatic compression (Figure 6d), cooling due to vertical temperature advection (Figure 6c), and cooling due to diabatic processes (primarily the net emission of longwave radiation; Figure 6e). This balance holds prior to extreme precipitation events between Day −12 and Day −3 (solid lines in Figures 6c–6e). The prevailing winds over the B-J region during winter are southwesterly owing to the mechanical splitting of the subtropical westerlies enforced by the TP. This southwesterly flow is associated with weak warm horizontal temperature advection prior to the development of the extreme events (from Day −12 to Day −3; solid line in Figure 6b).

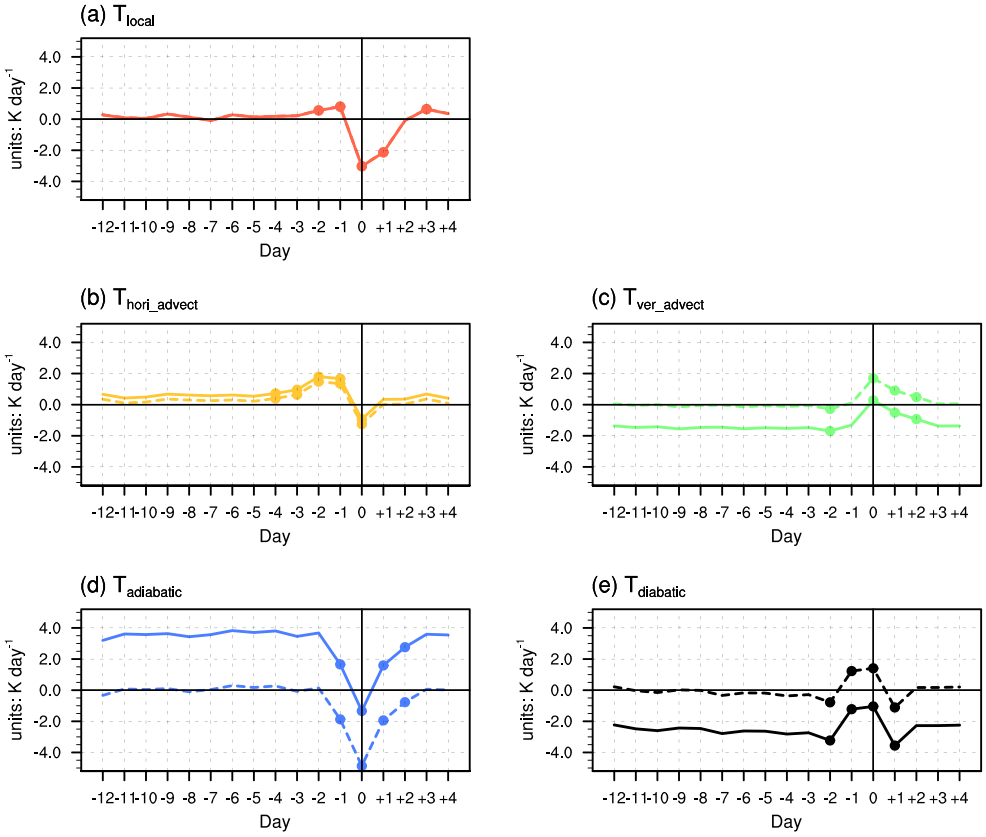


**Figure 6.** Composite evolution of (a) the area-averaged local temperature tendency ($T_{\text{local}}$) on the 850 hPa isobaric surface over the Balkhash-Junggar region, along with component contributions from (b) horizontal temperature advection ($T_{\text{hori}_a\text{dvect}}$), (c) vertical temperature advection ($T_{\text{ver}_a\text{dvect}}$), (d) adiabatic heating ($T_{\text{adiabatic}}$), and (e) diabatic heating ($T_{\text{diabatic}}$) from Day −12 to Day +4 at daily intervals around the 127 extreme precipitation events. All temperature tendencies are in units of K day$^{-1}$. Composite means are shown as solid lines and composite anomalies (relative to the corresponding DJF 1979–2017 climatologies) as dashed lines. Dots indicate that composite a nomalies are significant at 95% confidence level based on two-tailed Student's *t* tests.

To better isolate the impact of circulation anomalies associated with the development of the extreme precipitation events, we subtract the long-term mean for each term in the thermodynamic energy equation (Equation 2) over the B-J region during DJF 1979–2017 (dashed lines in Figure 6). Significant warming appears over the B-J region on Day −2 and Day −1, with magnitudes of 0.6 and 0.8 K day$^{-1}$, respectively (Figure 6a). The warming on Day −2 is primarily due to horizontal temperature advection (1.5 K day$^{-1}$; Figure 6b) resulting from enhanced southwesterly inflow driven by the approach of the lower-tropospheric cyclonic anomaly. Advective warming remains significant on Day −1 (Figure 6b) but is supplemented at this point by anomalous diabatic heating (1.2 K day$^{-1}$; Figure 6e). This diabatic heating anomaly is likely related to the combined effects of latent heat release due to precipitation formation and the inhibition of outgoing longwave radiation by extensive cloud cover. Our algorithm for identifying extreme precipitation events may miss the initial onset of precipitation if daily precipitation on that day does not meet the threshold for defining an extreme precipitation day. Therefore, the diabatic anomaly on Day −1 is still impacted by enhanced precipitation and deep convective cloud cover associated with the extreme precipitation event over the B-J region, even though it precedes the onset date according to our algorithm.

Strong cooling tendencies develop over the B-J region on Day 0 and Day +1, with magnitudes of −3.0 and −2.1 K day$^{-1}$ (Figure 6a). The cooling on Day 0 arises from the combined effects of adiabatic cooling due to strong updrafts (Figure 6d) and horizontal advective cooling (Figure 6b). On Day 0, the cyclonic anomaly related to extreme precipitation is centered to the northeast of the B-J region. As a consequence, northwesterly wind anomalies drive horizontal advective cooling over the B-J region on Day 0. The cooling on Day +1

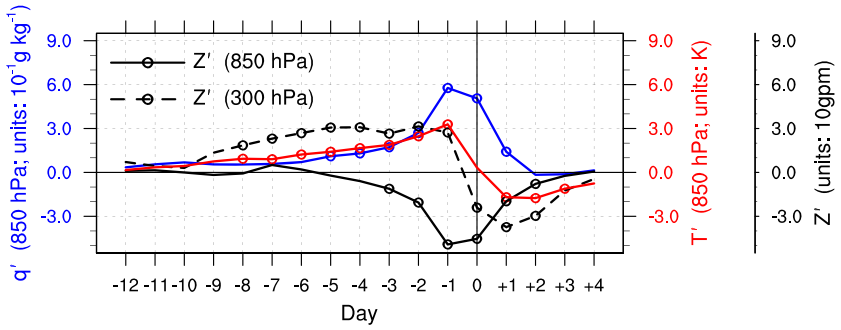


**Figure 7.** Composite evolution of area-averaged 850-hPa geopotential height anomalies (units: 10 gpm; black solid line), 300-hPa geopotential height anomalies (units: 10 gpm; black dashed line), 850-hPa specific humidity anomalies (units: $10^{-1}$ g kg$^{-1}$; blue line), and 850-hPa temperature anomalies (units: K; red line) over the Balkhash-Junggar region from Day −12 to Day +4 at daily intervals. Hollow circles indicate composite anomalies that are significant at 95% confidence level based on two-tailed Student's *t* tests.

results primarily from the combined effects of adiabatic cooling due to updrafts (Figure 6d) and diabatic cooling (Figure 6e). A considerable fraction of precipitation during these wintertime extreme precipitation events occurs in the form of snow (not shown). The diabatic cooling on Day +1 may be related to the melting of fresh snowfall after the occurrence of extreme precipitation.

In summary, horizontal advection and diabatic heating play critical roles in the warming of the B-J region before the onset of extreme precipitation events, while adiabatic cooling, horizontal advection, and diabatic processes all play important roles in the rapid cooling of the B-J region around the onset of extreme precipitation.

## 5. Moisture Sources for Extreme Precipitation

In this section, we explore the moisture sources for wintertime extreme precipitation events over the B-J region from both Lagrangian and Eulerian viewpoints.

### 5.1. Lagrangian Moisture Source Analysis

In this section, we use the Lagrangian moisture attribution method introduced in section 2.5 to identify the key moisture source regions. We further calculate characteristic timescales for moisture transport from each key moisture source region to the B-J region in the lead-up to extreme precipitation events.

#### 5.1.1. Key Moisture Source Regions

Figure 8a shows the mean horizontal distribution of moisture sources for the 127 identified wintertime extreme precipitation events over the B-J region. Regions with moisture contributions exceeding 0.002 mm day$^{-1}$ include the B-J region, terrestrial areas to the west and southwest of the B-J region, the northwestern Arabian Sea, and the North Atlantic Ocean. The largest contributors, with contributions exceeding 0.2 mm day$^{-1}$, are primarily situated southwest of the B-J region (northwest of the TP). This distribution of substantial moisture sources is consistent with horizontal moisture advection into the B-J region via the prevailing southwesterly winds during winter.

To quantify the relative moisture contributions from different regions to the precipitation over the B-J region during the 127 extreme events, we divide the latitude-longitude box bounded by 0°N–75°N and 60°W–100°E into 12 separate sectors (Figure 8b). When dividing the region, we have considered the horizontal distribution of moisture sources shown in Figure 8a. We only consider grid points with moisture contributions exceeding a set threshold (0.0059 mm day$^{-1}$), which collectively account for 95% of the total moisture contributed from anywhere on the globe (not only the region shown in the map). The sectors we consider include (1) central Asia, (2) the B-J region, (3) the Middle East, (4) Europe, (5) the TP, (6) northern Africa, (7) northwestern Asia, (8) the Aral and Caspian Seas, (9) the Mediterranean Sea, (10) the North Atlantic Ocean, (11) the Indian Ocean, and (12) the Black Sea. Sectors 1–7 are land regions, while Sectors 8–12 are maritime regions. Together, these 12 sectors contribute 94.1% of the moisture for precipitation during the 127 extreme events, demonstrating that all key moisture sources are accounted for in this list.

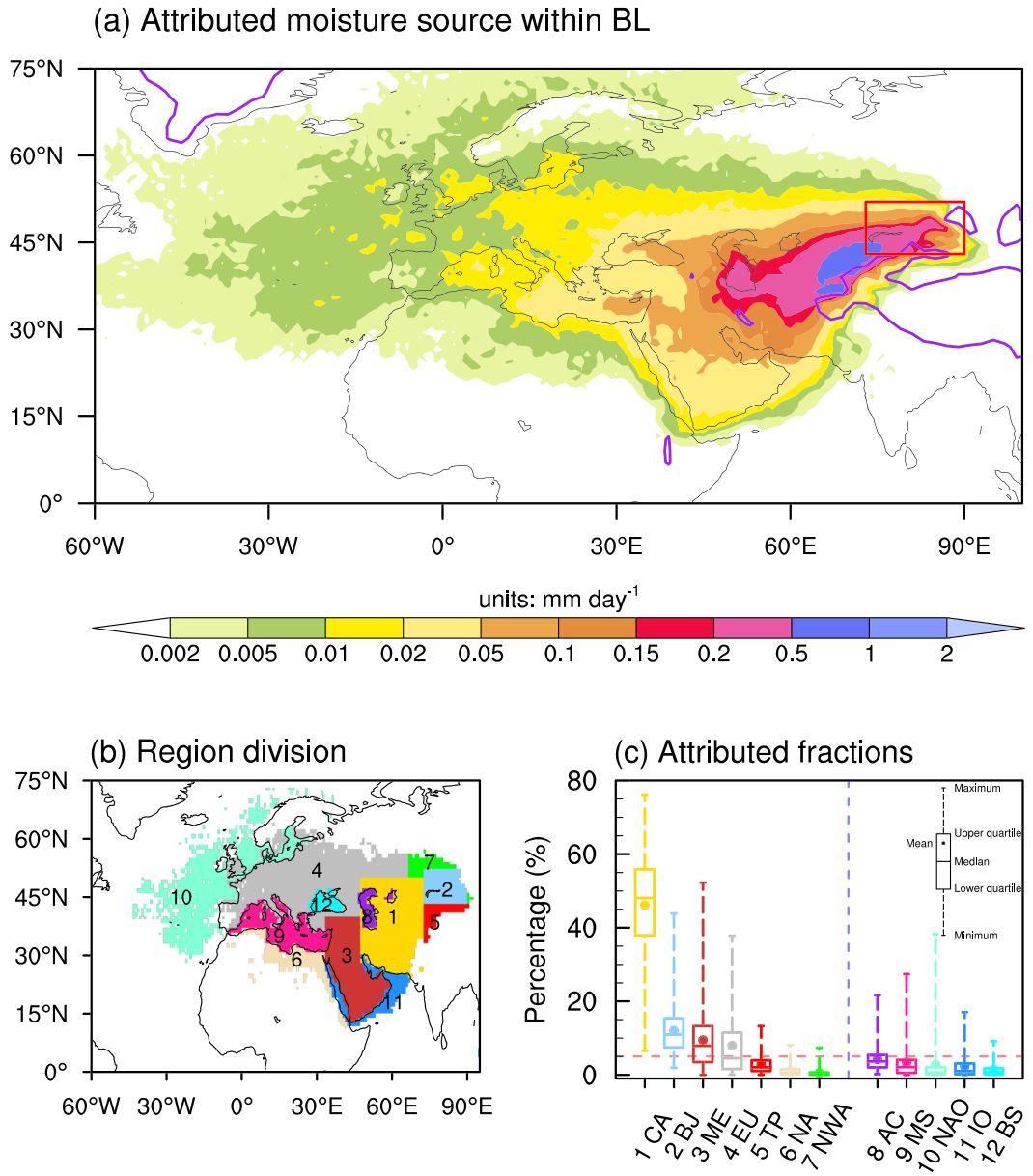


**Figure 8.** (a) The composite-mean horizontal distribution of attributed moisture sources (units: mm day$^{-1}$) for the 127 wintertime extreme precipitation events over the Balkhash-Junggar (B-J) region. The B-J region is marked by the red box, and regions with surface altitudes higher than 2,000 m are bounded by solid purple lines. (b) Categorical definition of the 12 sectors used to diagnose and attribute moisture sources, including (1) central Asia (CA), (2) the Balkhash-Junggar region (BJ), (3) the Middle East (ME), (4) Europe (EU), (5) the Tibetan Plateau (TP), (6) northern Africa (NA), (7) northwestern Asia (NWA), (8) the Aral and Caspian Seas (AC), (9) the Mediterranean Sea (MS), (10) the North Atlantic Ocean (NAO), (11) the Indian Ocean (IO), and (12) the Black Sea (BS). (c) Box-and-whisker diagram summarizing relative moisture contributions from each potential source sector to precipitation in the B-J region during the 127 extreme precipitation events.

Relative moisture contributions (or moisture contribution ratio) from each sector are calculated for each event as the ratio of the area integral of the contribution from that sector to the total contribution from all locations around the globe. Figure 8c shows box-and-whisker plots of relative moisture contributions from each of the 12 sectors across the 127 wintertime extreme precipitation events. In the box-and-whisker plot, the upper and bottom boundaries of each box represent the 75th and 25th percentiles, respectively, while the horizontal line through the box represents the median (50th percentile) across all 127 events. The top and

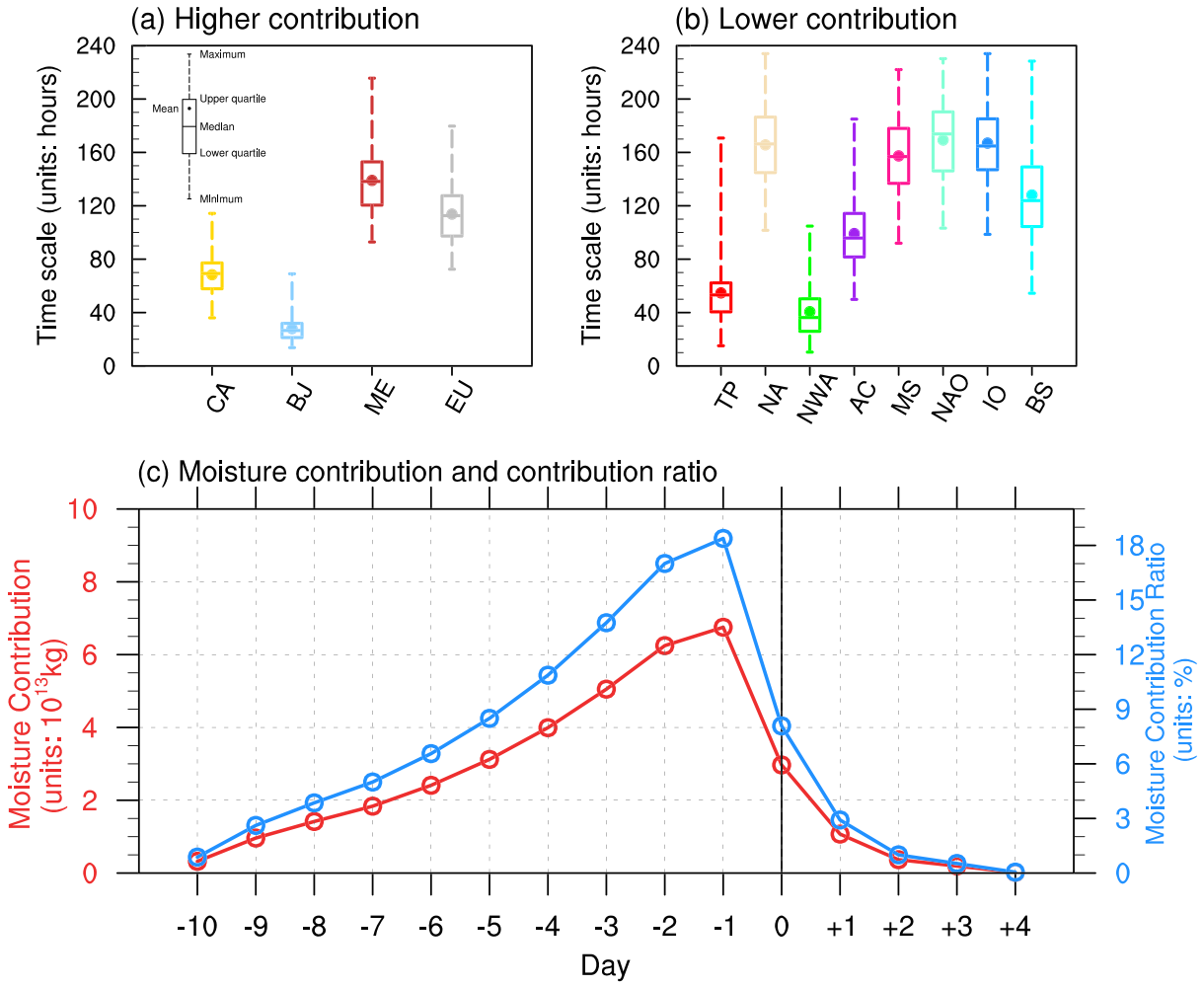


**Figure 9.** Box-and-whisker diagrams summarizing the characteristic timescales for moisture transport from (a) the four key moisture source regions and (b) the other eight moisture source regions to the Balkhash-Junggar (B-J) region for the 127 wintertime extreme precipitation events. (c) Composite daily evolution of globally integrated moisture contribution (units: $10^{13}$ kg; red line) and the contribution ratio of moisture uptake from that day (units: %; blue line) to the total moisture supply for wintertime extreme precipitation events between Day −10 and Day +4.

bottom whiskers mark the maximum and minimum contributions, while the dot marks the mean value. Key moisture source regions for extreme precipitation events over the B-J region are identified as regions with mean relative moisture contributions of 5% or more. Given this threshold, the four key moisture source regions are, in descending order: central Asia (46.2%), the B-J region (12.0%), the Middle East (9.5%), and Europe (8.0%). Note that the moisture contribution from the B-J region itself (12.0%) is less than those from other regions (88.0%). The relative moisture contributions from these four key moisture source regions exhibit large variations. Contributions from central Asia vary from 6.6% to 76.1%, while contributions from the B-J region vary from 2.0% to 43.9%. Contributions from the Middle East vary from 0.0% to 52.3%, while those from Europe vary from 0.1% to 37.8%. Mean relative moisture contributions from the other eight sectors are less than 5%. In total, the seven terrestrial sectors contribute 80.1% of the moisture for precipitation during the 127 extreme events, while the five maritime sectors contribute 14.0%.

### 5.1.2. Characteristic Timescales

Characteristic transport timescales can be estimated for moisture transport from each source region to the B-J region. We define the characteristic timescale for moisture transport as the weighted average of time elapsed between all moisture uptake episodes exceeding 0.01 mm day$^{-1}$ within the specified source region and the arrival of those air parcels at their precipitation locations within the B-J region. Here, a "precipitation location" is a location in the B-J region where a backward trajectory is initiated, provided the

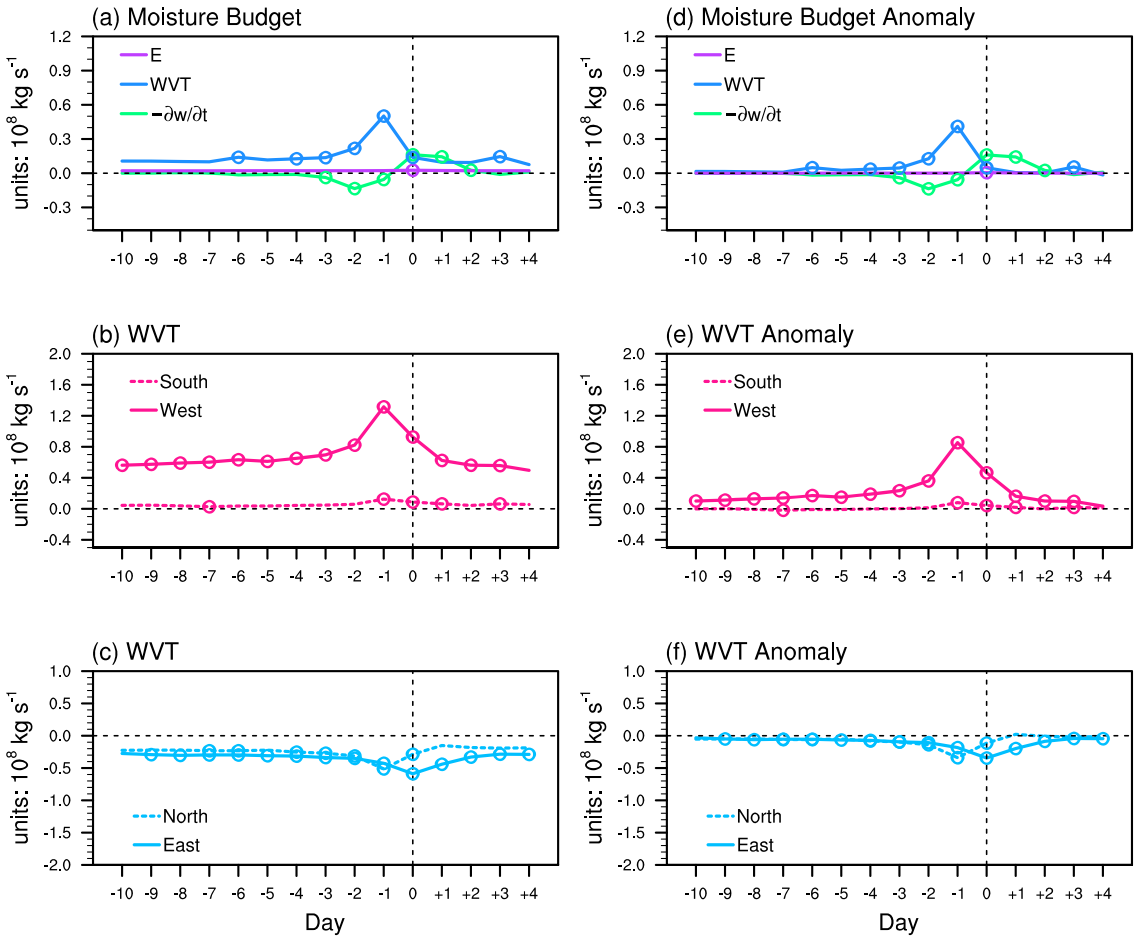


**Figure 10.** Composite evolution of (a) contributions to the precipitation over the Balkhash-Junggar region by three physical processes: the local tendency of precipitable water ($-\partial w/\partial t$), convergence of vertically integrated water vapor transport (WVT), and evapotranspiration (E), along with contributions based on (b) vertically integrated water vapor transport across the western and southern boundaries and (c) vertically integrated water vapor transport across the eastern and northern boundaries. Composite evolutions are shown for Day −10 to Day +4 at daily intervals around the 127 extreme precipitation events. All terms are shown in units of $10^8$ kg s$^{-1}$. Panels (d)–(f) show anomalies for the quantities in panels (a)–(c) relative to their average values during DJF 1979–2017. Hollow circles indicate composite anomalies that are significant at 95% confidence level based on two-tailed Student's *t* tests.

corresponding parcel meets the criteria for precipitation ($\Delta q_k^0 < 0$ and RH ≥ 70%; see section 2.5.2). For each moisture uptake location, the weight assigned for its contribution to the characteristic timescale is the magnitude of the estimated moisture uptake.

The mean characteristic timescales for moisture transport from the key moisture source regions are 2.8 days from central Asia, 1.2 days from the B-J region, 5.8 days from the Middle East, and 4.7 days from Europe (Figure 9a). The largest moisture contributor, central Asia, has characteristic timescales ranging from 1.5 to 4.8 days across different extreme precipitation events. Characteristic timescales for moisture transport from the eight source regions with mean contribution ratios smaller than 5% are shown in Figure 9b.

Figure 9c shows the composite-mean temporal evolution of the globally integrated moisture contributions (in kg) and the corresponding contribution ratios between Day −10 and Day +4. The contribution ratio for each day is calculated as the ratio of the global integral of moisture contributions on that day to the total moisture contribution over Day −10 through Day +4. The existence of moisture contributions between Day +1 and Day +4 reflects the fact that the extreme precipitation events had lifetimes of up to 5 days. However, because these longer events are relatively uncommon, the cumulative contribution ratio from these last 4 days is only 4.5%, indicating that moisture contributions during this extended period play negligible roles in the overall moisture supply for extreme precipitation events over the B-J region. Only 4 days have mean moisture contribution ratios greater than 10%: Day −4 (10.9%), Day −3 (13.8%), Day −2 (17.0%), and Day −1

(18.4%). The majority (60.1%) of moisture for extreme precipitation events over the B-J region during extreme events is therefore linked to evapotranspiration that occurs within 1–4 days prior to the onset of the events. This result is consistent with moisture transport from the largest moisture source region (central Asia) having characteristic transport timescales ranging from 1.5 to 4.8 days.

### 5.2. Eulerian Moisture Budget Analysis

Figure 10a displays the composite evolution of area-weighted contributions from the three terms on the right-hand side of Equation 6 to precipitation between Day −10 and Day +4 around the 127 extreme precipitation events over the B-J region. Figure 10d shows anomalies for the same three terms relative to their climatological means during DJF 1979–2017. The ratio of the cumulative contribution from large-scale moisture convergence to that from local evapotranspiration is 6.7 for Day −10 through Day +4 (Figure 10a). The Lagrangian moisture source analysis likewise indicates that the ratio between moisture contributions from regions outside the B-J region (88.0%) to moisture contributions from the B-J region itself (12.0%) is 7.3 over the same period (Figure 8c). Therefore, both approaches consistently show that local evapotranspiration is less influential than large-scale moisture convergence in supplying moisture for wintertime extreme precipitation over the B-J region, by a factor of around 7. The contribution from large-scale moisture convergence is only around $0.1 \times 10^8$ kg s$^{-1}$ prior to Day −2 but rapidly doubles to $0.2 \times 10^8$ kg s$^{-1}$ on Day −2. This doubling of the large-scale moisture convergence term coincides with the arrival of the lower-tropospheric cyclonic anomaly at the northwestern edge of the B-J region (Figure 5b). Moisture convergence reaches a peak value of $0.5 \times 10^8$ kg s$^{-1}$ on Day −1, as the cyclonic anomaly continues its eastward migration. As discussed in section 4.2, significant warming occurs in the lower troposphere over the B-J region on Day −2 and Day −1 due to the position and movement of the cyclonic anomaly, with 850-hPa temperature anomalies exceeding 2 K on both days (Figure 7). According to the Clausius-Clapeyron relationship, saturation specific humidity increases with temperature at a rate of approximately 7% K$^{-1}$ in Earth's present-day atmosphere (Held & Soden, 2006; O'Gorman & Muller, 2010; Trenberth et al., 2003). The warming thus allows a considerable fraction of the enhanced large-scale moisture convergence to be transformed into precipitable water, resulting in precipitable water tendencies of $0.13 \times 10^8$ kg s$^{-1}$ on Day −2 and $0.06 \times 10^8$ kg s$^{-1}$ on Day −1. The rapid cooling on Day 0 and Day +1 (as discussed in section 4.2) sharply reduces saturation specific humidity over the B-J region. This rapid cooling thus transforms a considerable fraction of the precipitable water into precipitation, resulting in precipitable water tendencies of $-0.16 \times 10^8$ kg s$^{-1}$ on Day 0 and $-0.14 \times 10^8$ kg s$^{-1}$ on Day +1. It is worth noting that the cumulative change in moisture contributed by variations in precipitable water over the entire period is only about $0.06 \times 10^{13}$ kg, much smaller than the $1.90 \times 10^{13}$ kg contributed by large-scale moisture convergence.

Figures 10b and 10c show the temporal evolution of moisture fluxes across the four lateral boundaries of the B-J region for Day −10 to Day +4 around the 127 extreme precipitation events. Moisture fluxes across the western and southern boundaries are positive throughout the period, while those across the eastern and northern boundaries are negative. These moisture fluxes are consistent with the southwesterly winds that prevail in this region during winter. However, the cumulative moisture flux entering the B-J region across the western boundary over this 15-day period is $8.8 \times 10^{13}$ kg, more than an order of magnitude larger than that entering across the southern boundary ($0.7 \times 10^{13}$ kg). The much weaker moisture transport across the southern boundary is attributable to the presence of the high-altitude TP to the south of the B-J region, which blocks moisture inflow from this direction.

To summarize, large-scale moisture convergence plays the dominant role in supplying moisture for extreme precipitation events over the B-J region, with most of the moisture for precipitation entering the region across the western boundary. Variations in temperature are favorable for moisture accumulation over the B-J region during the days immediately prior to extreme events but unfavorable after the events begin. Variations in precipitable water therefore contribute to the enhanced intensity of precipitation during the extreme events.

## 6. Summary and Concluding Remarks

In this study, we have examined the formation mechanisms for wintertime extreme precipitation events over the Balkhash-Junggar (B-J) region during DJF 1979–2017. An upper-tropospheric Rossby wave train forms

on average 6 days before the onset of these events, with four centers of action that extend from the North Atlantic Ocean to the B-J region. This Rossby wave train slowly migrates eastward under the steering influence of the midlatitude westerlies. At the onset of the extreme precipitation events, a dipole pattern consisting of a cyclonic anomaly (northwest of the B-J region) and an anticyclonic anomaly (southeast of the B-J region) is evident in the upper troposphere above the B-J region. These anomalies are the two easternmost centers of action in the upper-tropospheric Rossby wave train. The Rossby wave train is also evident in the lower troposphere, although the easternmost cyclonic anomaly in the lower troposphere moves faster than its counterpart in the upper troposphere. As a consequence, the B-J region is covered by a lower-tropospheric cyclonic anomaly around the onset time of an extreme precipitation event. This cyclonic anomaly not only favors strong updrafts over the B-J region but also enhances the prevailing southwesterly winds that represent the primary moisture supply to the B-J region.

When identifying the extreme precipitation events, a nonextreme precipitation day is allowed to exist between two extreme precipitation days. Even after this relaxation of the criteria, almost all days (92.7%) during the identified events still qualify as extreme precipitation days (i.e., days with precipitation exceeding 2.22 mm day$^{-1}$). A set of sensitivity experiments are conducted to investigate whether the definition of extreme events affects the identification of favorable circulation patterns for extreme precipitation in the B-J region. These sensitivity experiments include (A) one nonextreme precipitation day is allowed to exist prior to the first extreme precipitation day; (B) one nonextreme precipitation day is allowed to exist after the last extreme precipitation day; (C) one nonextreme precipitation day is allowed to exist between two extreme precipitation days, but with the 3-day running mean precipitation used to define extreme precipitation events; and (D) same as (C) but no nonextreme precipitation days are allowed. The evolution of composite geopotential height anomalies on the 300 hPa isobaric surface from Day −6 to Day −2 under each of these sensitivity experiments is shown in Figure S6. The results all show a significant Rossby wave train extending from the North Atlantic to the B-J region on Day −4, similar to the Rossby wave train shown in Figure 3e. The favorable circulation pattern we identify is therefore qualitatively insensitive to these adjustments in our definition of extreme precipitation events. However, the percentages of days with precipitation exceeding 2.22 mm day$^{-1}$ among the days selected under Experiments (A)–(D) are 55.7%, 55.7%, 54.9%, and 53.7%, respectively, far less than that under our selected definition (92.7%). Our definition thus better accentuates the conditions associated with the occurrence of extreme precipitation in the B-J region.

The lower troposphere above the B-J region warms in the days immediately before an extreme precipitation event and then cools rapidly after the onset of the event. The warming before onset arises from both horizontal temperature advection downstream of the lower-tropospheric cyclonic anomaly and diabatic heating related to cloud radiative effects. The rapid cooling just after onset can be attributed to adiabatic cooling associated with the strong updrafts, horizontal advection upstream of the lower-tropospheric cyclonic anomaly, and diabatic effects related to the melting of surface snow.

Lagrangian moisture source attribution analysis reveals four key moisture source regions for precipitation in the B-J region during these extreme precipitation events. These regions are, in order of decreasing importance: central Asia (46.2%), the B-J region itself (12.0%), the Middle East (9.5%), and Europe (8.0%). The characteristic timescales for moisture transport from these four source regions range from 1 day to 1 week. The dominant role of central Asia in supplying moisture for wintertime extreme precipitation events is linked to the enhancement of prevailing southwesterly winds around the onset of these extreme events. The majority (60.1%) of moisture for precipitation during these events can be linked to moisture uptake that occurs between 1 and 4 days prior to the event. The backward integration timescale used in the Lagrangian analysis is set to 10 days. Recently, Nieto and Gimeno (2019) developed a database of optimal backward integration timescales for Lagrangian analysis of atmospheric moisture sources and sinks by comparing precipitation estimates from the Lagrangian approach across a range of backward integration timescales. Based on their database, the optimal backward integration timescale for the B-J region during winter is about 6.3 days. As shown in Figure 9c, most (~83.3%) of the moisture uptakes preceding extreme precipitation events over the B-J region occur between Day −6 and Day 0, consistent with the optimal timescale suggested by Nieto and Gimeno (2019).

Eulerian moisture budget analysis indicates that the lower-tropospheric temperature variations play a key role in moisture changes as well. The initial warming prior to the onset of extreme precipitation promotes

the accumulation of precipitable water over the B-J region, while the subsequent rapid cooling acts to transform excess precipitable water into precipitation. The Eulerian moisture budget analysis also reveals that the moisture supply for extreme precipitation events over the B-J region is contributed mainly by large-scale moisture convergence.

This study illustrates the formation mechanisms for wintertime extreme precipitation events over a typical arid/semiarid area from two different viewpoints. The Rossby wave train that extends from the North Atlantic Ocean to the B-J region constitutes the favorable circulation pattern for extreme precipitation, as this wave train leads to stronger southwesterly winds, moisture convergence, ascending motion, and the sequence of temperature variation that favors the accumulation and subsequent release of precipitable water over the B-J region. Given this dynamical backdrop, we identify and quantify the moisture sources for the resulting extreme precipitation events, finding that terrestrial regions, especially central Asia, contribute most of the moisture for the extreme events. These findings are of fundamental importance to the prediction of extreme precipitation events over the B-J region.

There are several outstanding issues that remain to be addressed in further study. First, we have identified and described the favorable circulation patterns via composite analysis. However, the favorable circulation patterns associated with each of the 127 extreme precipitation events may differ in important ways relative to the composite mean. For example: Does the Rossby wave train actually occur in most or all extreme precipitation events? To be certain, it will be necessary to classify the circulation patterns among the 127 extreme precipitation events. Second, among the influencing factors that we highlight in this work (such as the lower-tropospheric cyclonic anomaly over the B-J region, the Rossby wave train, increased southwesterly winds, temperature variations, moisture convergence, and strong ascent), what are the unique factors that trigger the formation of extreme precipitation rather than moderate precipitation? Third, the orographic effects of the TP, the Tianshan Mountains, and the Altai Mountains may play essential roles that are not fully recognized in this study. Would the favorable circulation pattern still lead to extreme precipitation over a region like the B-J region without these orographic effects? These issues are beyond the scope of this study and will require further investigation as we work to better understand the mechanisms involved in the formation of wintertime extreme precipitation events over the B-J region and other dryland regions.

## Data Availability Statement

The ERA-Interim reanalysis data set is available online (from https://www.ecmwf.int/en/forecasts/datasets/reanalysis-datasets/era-interim). The JRA55 precipitation data set is available online (from https://jra.kishou.go.jp/JRA-55/index_en.html). The MERRA precipitation data set is available online (from https://gmao.gsfc.nasa.gov/reanalysis/MERRA/).

**Acknowledgments**
We thank the editor and anonymous reviewers for their constructive comments that led to the improvement of the manuscript. This work was jointly supported by the National Natural Science Foundation of China (91737307) and Tsinghua University Initiative Scientific Research Program (2019Z07L02011).

## References

An, D., & Zhao, J. (2013). An infrequent snowstorm weather over the central Tianshan Mountains in Xinjiang [in Chinese]. *Arid Zone Research*, *30*(3), 470–476. https://doi.org/10.13866/j.azr.2013.03.023

Cao, Y., Nan, Z., Cheng, G., & Zhang, L. (2018). Hydrological variability in the arid region of Northwest China from 2002 to 2013. *Advances in Meteorology*, *2018*, 13. https://doi.org/10.1155/2018/1502472

Chen, Y., Deng, H., Li, B., Li, Z., & Xu, C. (2014). Abrupt change of temperature and precipitation extremes in the arid region of Northwest China. *Quaternary International*, *336*, 35–43. https://doi.org/10.1016/j.quaint.2013.12.057

Chen, B., Xu, X. D., Yang, S., & Zhang, W. (2012). On the origin and destination of atmospheric moisture and air mass over the Tibetan Plateau. *Theoretical and Applied Climatology*, *110*(3), 423–435. https://doi.org/10.1007/s00704-012-0641-y

Dai, A. (2011). Drought under global warming: A review. *Wiley Interdisciplinary Reviews: Climate Change*, *2*(1), 45–65. https://doi.org/10.1002/wcc.81

Dai, A. (2012). Increasing drought under global warming in observations and models. *Nature Climate Change*, *3*, 52–58. https://doi.org/10.1038/nclimate1633

Dai, X., Li, W., Ma, Z., & Wang, P. (2007). Water-vapor source shift of Xinjiang region during the recent twenty years. *Progress in Natural Science*, *17*(5), 569–575. https://doi.org/10.1080/10020070708541037

Dai, A., & Zhao, T. (2017). Uncertainties in historical changes and future projections of drought. Part I: Estimates of historical drought changes. *Climatic Change*, *144*(3), 519–533. https://doi.org/10.1007/s10584-016-1705-2

Dee, D. P., Uppala, S. M., Simmons, A. J., Berrisford, P., Poli, P., Kobayashi, S., et al. (2011). The ERA-Interim reanalysis: Configuration and performance of the data assimilation system. *Quarterly Journal of the Royal Meteorological Society*, *137*(656), 553–597. https://doi.org/10.1002/qj.828

Dole, R. M., & Black, R. X. (1990). Life cycles of persistent anomalies. Part II: The development of persistent negative height anomalies over the North Pacific Ocean. *Monthly Weather Review*, *118*(4), 824–846. https://doi.org/10.1175/1520-0493(1990)118 <0824:LCOPAP>2.0.CO;2

Drumond, A., Nieto, R., & Gimeno, L. (2011). Sources of moisture for China and their variations during drier and wetter conditions in 2000–2004: A Lagrangian approach. *Climate Research*, *50*, 215–225. https://doi.org/10.3354/cr01043

Drumond, A., Nieto, R., Hernández, E., & Gimeno, L. (2011). A Lagrangian analysis of the variation in moisture sources related to drier and wetter conditions in regions around the Mediterranean Basin. *Natural Hazards and Earth System Sciences*, *11*(8), 2307–2320. https://doi.org/10.5194/nhess-11-2307-2011

Durán-Quesada, A. M., Gimeno, L., Amador, J. A., & Nieto, R. (2010). Moisture sources for Central America: Identification of moisture sources using a Lagrangian analysis technique. *Journal of Geophysical Research*, *115*, D05103. https://doi.org/10.1029/2009JD012455

Feng, S., & Fu, Q. (2013). Expansion of global drylands under a warming climate. *Atmospheric Chemistry and Physics*, *13*(19), 10,081–10,094. https://doi.org/10.5194/acp-13-10081-2013

Gimeno, L., Drumond, A., Nieto, R., Trigo, R. M., & Stohl, A. (2010). On the origin of continental precipitation. *Geophysical Research Letters*, *37*, L13804. https://doi.org/10.1029/2010GL043712

Gimeno, L., Stohl, A., Trigo, R. M., Dominguez, F., Yoshimura, K., Yu, L., et al. (2012). Oceanic and terrestrial sources of continental precipitation. *Reviews of Geophysics*, *50*, RG4003. https://doi.org/10.1029/2012RG000389

Guan, X., Huang, J., Guo, R., Yu, H., Lin, P., & Zhang, Y. (2015). Role of radiatively forced temperature changes in enhanced semi-arid warming in the cold season over east Asia. *Atmospheric Chemistry and Physics*, *15*(23), 13,777–13,786. https://doi.org/10.5194/acp-15 - 13777-2015

Held, I. M., & Soden, B. J. (2006). Robust responses of the hydrological cycle to global warming. *Journal of Climate*, *19*(21), 5686–5699. https://doi.org/10.1175/JCLI3990.1

Howland, M. R., & Sikdar, D. N. (1983). The moisture budget over the northeastern Arabian Sea during premonsoon and monsoon onset, 1979. *Monthly Weather Review*, *111*(11), 2255–2268. https://doi.org/10.1175/1520-0493(1983)111<2255:TMBOTN>2.0.CO;2

Hua, L., Zhong, L., & Ma, Z. (2017). Decadal transition of moisture sources and transport in northwestern China during summer from 1982 to 2010. *Journal of Geophysical Research: Atmospheres*, *122*, 12,522–12,540. https://doi.org/10.1002/2017JD027728

Huang, W., Chang, S., Xie, C., & Zhang, Z. (2017). Moisture sources of extreme summer precipitation events in North Xinjiang and their relationship with atmospheric circulation. *Advances in Climate Change Research*, *8*(1), 12–17. https://doi.org/10.1016/j.accre.2017.02.001

Huang, J., Ji, M., Xie, Y., Wang, S., He, Y., & Ran, J. (2016). Global semi-arid climate change over last 60 years. *Climate Dynamics*, *46*(3), 1131–1150. https://doi.org/10.1007/s00382-015-2636-8

Huang, J., Li, Y., Fu, C., Chen, F., Fu, Q., Dai, A., et al. (2017). Dryland climate change: Recent progress and challenges. *Reviews of Geophysics*, *55*, 719–778. https://doi.org/10.1002/2016RG000550

Huang, J., Yu, H., Guan, X., Wang, G., & Guo, R. (2016). Accelerated dryland expansion under climate change. *Nature Climate Change*, *6*, 166–171. https://doi.org/10.1038/nclimate2837

Ionita, M., Scholz, P., & Chelcea, S. (2016). Assessment of droughts in Romania using the Standardized Precipitation Index. *Natural Hazards*, *81*(3), 1483–1498. https://doi.org/10.1007/s11069-015-2141-8

James, P., Stohl, A., Spichtinger, N., Eckhardt, S., & Forster, C. (2004). Climatological aspects of the extreme European rainfall of August 2002 and a trajectory method for estimating the associated evaporative source regions. *Natural Hazards and Earth System Sciences*, *4*(5/6), 733–746. https://doi.org/10.5194/nhess-4-733-2004

Ji, M., Huang, J., Xie, Y., & Liu, J. (2015). Comparison of dryland climate change in observations and CMIP5 simulations. *Advances in Atmospheric Sciences*, *32*(11), 1565–1574. https://doi.org/10.1007/s00376-015-4267-8

Jin, F., & Zangvil, A. (2009). Relationship between moisture budget components over the eastern Mediterranean. *International Journal of Climatology*, *30*, 733–742. https://doi.org/10.1002/joc.1911

Kim, H. M., Zhou, Y., & Alexander, M. A. (2019). Changes in atmospheric rivers and moisture transport over the Northeast Pacific and western North America in response to ENSO diversity. *Climate Dynamics*, *52*(12), 7375–7388. https://doi.org/10.1007/s00382-017-3598-9

Kobayashi, S., Ota, Y., Harada, Y., Ebita, A., Moriya, M., Onoda, H., et al. (2015). The JRA-55 reanalysis: General specifications and basic characteristics. *Journal of the Meteorological Society of Japan*, *93*(1), 5–48. https://doi.org/10.2151/jmsj.2015-001

Li, Q., Chen, Y., Shen, Y., Li, X., & Xu, J. (2011). Spatial and temporal trends of climate change in Xinjiang, China. *Journal of Geographical Sciences*, *21*(6), 1007. https://doi.org/10.1007/s11442-011-0896-8

Li, B., Chen, Y., & Shi, X. (2012). Why does the temperature rise faster in the arid region of northwest China. *Journal of Geophysical Research*, *117*, D16115. https://doi.org/10.1029/2012JD017953

Li, Y., Huang, J., Ji, M., & Ran, J. (2015). Dryland expansion in northern China from 1948 to 2008. *Advances in Atmospheric Sciences*, *32*(6), 870–876. https://doi.org/10.1007/s00376-014-4106-3

Li, Y., Shavket, D., Yang, L., & Zhang, Y. (2014). Analysis on a heavy snow by central Asian vortex in Xinjiang [in Chinese]. *Scientia Meteorologica Sinica*, *34*(3), 299–304. https://doi.org/10.3969/2013jms.0085

Li, R., Tang, Y., & Rouzi, A. (2015). Atmospheric circulation and water vapor characteristics of snowstorm anomalies in northern Xinjiang in 2010 [in Chinese]. *Plateau Meteorology*, *34*(1), 155–162. https://doi.org/10.7522/j.issn.1000-0534.2013.00163

Lin, X., Song, P., & Xia, Z. (1991). Dynamical calculation of typhoon heavy rain caused by baroclinic energy conversion [in Chinese]. *Tropic Oceanology*, *10*(3), 86–90.

Ling, J., & Zhang, C. (2013). Diabatic heating profiles in recent global reanalyses. *Journal of Climate*, *26*(10), 3307–3325. https://doi.org/10.1175/JCLI-D-12-00384.1

Ling, J., Zhang, C., & Bechtold, P. (2013). Large-scale distinctions between MJO and non-MJO convective initiation over the tropical Indian Ocean. *Journal of the Atmospheric Sciences*, *70*(9), 2696–2712. https://doi.org/10.1175/JAS-D-13-029.1

Liu, H., Cui, C., & Li, R. (2011). Analysis on a continuous snowstorm process over North Xinjiang in early January 2010 [in Chinese]. *Arid Zone Research*, *28*(2), 282–287. https://doi.org/10.13866/j.azr.2011.02.025

McKee, T., Doesken, N., & Kleist, J. (1993, January). *The relationship of drought frequency and duration to time scales*. Paper presented at 8th Conference on Applied Climatology, American Meteorological Society, Anaheim, California.

McKee, T., Doesken, N., & Kleist, J. (1995, January). *Drought Monitoring with Multiple Time Scales*. Paper presented at 9th Conference on Applied Climatology, American Meteorological Society, Dallas, Texas.

Mike, H. (1996). Recent climatic change in the world's drylands. *Geophysical Research Letters*, *23*(1), 61–64. https://doi.org/10.1029/95GL03586

Nieto, R., & Gimeno, L. (2019). A database of optimal integration times for Lagrangian studies of atmospheric moisture sources and sinks. *Scientific Data*, *6*(1), 59. https://doi.org/10.1038/s41597-019-0068-8

O'Gorman, P. A., & Muller, C. J. (2010). How closely do changes in surface and column water vapor follow Clausius–Clapeyron scaling in climate change simulations? *Environmental Research Letters*, *5*(2), 25207. https://doi.org/10.1088/1748-9326/5/2/025207

Peixoto, J. P., & Oort, A. H. (1992). *Physics of climate* (pp. 520). New York, NY: American Institute of Physics.
Peng, D., & Zhou, T. (2017). Why was the arid and semiarid northwest China getting wetter in the recent decades? *Journal of Geophysical Research: Atmospheres*, *122*, 9060–9075. https://doi.org/10.1002/2016JD026424
Peterson, T. C., Zhang, X., Brunet-India, M., & Vázquez-Aguirre, J. L. (2008). Changes in North American extremes derived from daily weather data. *Journal of Geophysical Research*, *113*, D07113. https://doi.org/10.1029/2007JD009453
Qian, Z., Wu, T., Song, M., Ma, X., Cai, Y., & Liang, X. (2001). Arid disaster and advances in arid climate researched over northwest China. *Advances in Earth Science*, *16*(1), 28. https://doi.org/10.11867/j.issn.1001-8166.2001.01.0028
Reynolds, J. F., Smith, D. M. S., Lambin, E. F., Turner, B. L., Mortimore, M., Batterbury, S. P. J., et al. (2007). Global desertification: Building a science for dryland development. *Science*, *316*(5826), 847–851. https://doi.org/10.1126/science.1131634
Rienecker, M. M., Suarez, M. J., Gelaro, R., Todling, R., Bacmeister, J., Liu, E., et al. (2011). MERRA: NASA's Modern-Era Retrospective Analysis for Research and Applications. *Journal of Climate*, *24*(14), 3624–3648. https://doi.org/10.1175/JCLI-D-11-00015.1
Salih, A. A. M., Zhang, Q., & Tjernström, M. (2015). Lagrangian tracing of Sahelian Sudan moisture sources. *Journal of Geophysical Research: Atmospheres*, *120*, 6793–6808. https://doi.org/10.1002/2015JD023238
Scheff, J., & Frierson, D. M. W. (2014). Scaling potential evapotranspiration with greenhouse warming. *Journal of Climate*, *27*(4), 1539–1558. https://doi.org/10.1175/JCLI-D-13-00233.1
Sherwood, S., & Fu, Q. (2014). A drier future? *Science*, *343*(6172), 737–739. https://doi.org/10.1126/science.1247620
Shi, Y., Liu, C., & Kang, E. (2009). The glacier inventory of China. *Annals of Glaciology*, *50*(53), 1–4. https://doi.org/10.3189/172756410790595831
Shi, Y., Shen, Y., Kang, E., Li, D., Ding, Y., Zhang, G., & Hu, R. (2007). Recent and future climate change in northwest China. *Climate Dynamics*, *80*(3), 379–393. https://doi.org/10.1007/s10584-006-9121-7
Simmonds, I., Bi, D., & Hope, P. (1999). Atmospheric water vapor flux and its association with rainfall over China in summer. *Journal of Climate*, *12*, 1353–1367. https://doi.org/10.1175/1520-0442(1999)012<1353:AWVFAI>2.0.CO;2
Sodemann, H., Schwierz, C., & Wernli, H. (2008). Interannual variability of Greenland winter precipitation sources: Lagrangian moisture diagnostic and North Atlantic Oscillation influence. *Journal of Geophysical Research*, *113*, D03107. https://doi.org/10.1029/2007JD008503
Sprenger, M., & Wernli, H. (2015). The LAGRANTO Lagrangian analysis tool—Version 2.0. *Geoscientific Model Development*, *8*(8), 2569–2586. https://doi.org/10.5194/gmd-8-2569-2015
Stohl, A., Forster, C., & Sodemann, H. (2008). Remote sources of water vapor forming precipitation on the Norwegian west coast at 60°N—A tale of hurricanes and an atmospheric river. *Journal of Geophysical Research*, *113*, D05102. https://doi.org/10.1029/2007JD009006
Stohl, A., & James, P. (2004). A Lagrangian analysis of the atmospheric branch of the global water cycle. Part I: Method description, validation, and demonstration for the August 2002 flooding in central Europe. *Journal of Hydrometeorology*, *5*(4), 656–678. https://doi.org/10.1175/1525-7541(2004)005<0656:ALAOTA>2.0.CO;2
Stohl, A., & James, P. (2005). A Lagrangian analysis of the atmospheric branch of the global water cycle. Part II: Moisture transports between Earth's ocean basins and river catchments. *Journal of Hydrometeorology*, *6*(6), 961–984. https://doi.org/10.1175/JHM470.1
Sun, B., & Wang, H. (2014). Moisture sources of semiarid grassland in China using the Lagrangian particle model FLEXPART. *Journal of Climate*, *27*(6), 2457–2474. https://doi.org/10.1175/JCLI-D-13-00517.1
Takaya, K., & Nakamura, H. (2001). A formulation of a phase-independent wave-activity flux for stationary and migratory quasigeostrophic eddies on a zonally varying basic flow. *Journal of the Atmospheric Sciences*, *58*(6), 608–627. https://doi.org/10.1175/1520-0469(2001)058<0608:AFOAPI>2.0.CO;2
Tiwari, S., Kar, S. C., & Bhatla, R. (2017). Atmospheric moisture budget during winter seasons in the western Himalayan region. *Climate Dynamics*, *48*(3), 1277–1295. https://doi.org/10.1007/s00382-016-3141-4
Trenberth, K. E. (1998). Atmospheric moisture residence times and cycling: Implications for rainfall rates and climate change. *Climatic Change*, *39*(4), 667–694. https://doi.org/10.1023/A:1005319109110
Trenberth, K. E. (1999). Atmospheric moisture recycling: Role of advection and local evaporation. *Journal of Climate*, *12*(5), 1368–1381. https://doi.org/10.1175/1520-0442(1999)012<1368:AMRROA>2.0.CO;2
Trenberth, K. E. (2011). Changes in precipitation with climate change. *Climate Research*, *47*(1-2), 123–138. https://doi.org/10.3354/cr00953
Trenberth, K. E., Dai, A., Rasmussen, R. M., & Parsons, D. B. (2003). The changing character of precipitation. *Bulletin of the American Meteorological Society*, *84*(9), 1205–1217. https://doi.org/10.1175/BAMS-84-9-1205
Trenberth, K. E., & Guillemot, C. J. (1995). Evaluation of the global atmospheric moisture budget as seen from analyses. *Journal of Climate*, *8*(9), 2255–2272. https://doi.org/10.1175/1520-0442(1995)008<2255:EOTGAM>2.0.CO;2
Vazquez, M., Nieto, R., Drumond, A., & Gimeno, L. (2016). Moisture transport into the Arctic: Source-receptor relationships and the roles of atmospheric circulation and evaporation. *Journal of Geophysical Research: Atmospheres*, *121*, 13,493–13,509. https://doi.org/10.1002/2016JD025400
Wang, H., Chen, Y., & Chen, Z. (2013). Spatial distribution and temporal trends of mean precipitation and extremes in the arid region, northwest of China, during 1960–2010. *Hydrological Processes*, *27*(12), 1807–1818. https://doi.org/10.1002/hyp.9339
Wang, S., Zhang, M., Jagoda, C., Hughes, C. E., Du, M., Du, M., & Liu, X. (2017). The effect of moisture source and synoptic conditions on precipitation isotopes in arid central Asia. *Journal of Geophysical Research: Atmospheres*, *122*, 2667–2682. https://doi.org/10.1002/2015JD024626
Wernli, B. H., & Davies, H. C. (1997). A Lagrangian-based analysis of extratropical cyclones. I: The method and some applications. *Quarterly Journal of the Royal Meteorological Society*, *123*(538), 467–489. https://doi.org/10.1002/qj.49712353811
Winschall, A., Pfahl, S., Sodemann, H., & Wernli, H. (2014). Comparison of Eulerian and Lagrangian moisture source diagnostics—The flood event in eastern Europe in May 2010. *Atmospheric Chemistry and Physics*, *14*, 6605–6619. https://doi.org/10.5194/acp-14-6605-2014
Yao, J., Li, M., & Yang, Q. (2018). Moisture sources of a torrential rainfall event in the arid region of East Xinjiang, China, based on a Lagrangian model. *Natural Hazards*, *92*(1), 183–195. https://doi.org/10.1007/s11069-018-3386-9
Zhang, X., Alexander, L., Hegerl, G. C., Jones, P., Tank, A. K., Peterson, T. C., et al. (2011). Indices for monitoring changes in extremes based on daily temperature and precipitation data. *WIREs Climate Change*, *2*(6), 851–870. https://doi.org/10.1002/wcc.147
Zhang, J., Cui, C., & Chen, C. (2013). Study on water vapor characteristic of typical heavy snowstorm case in Northern Xinjiang [in Chinese]. *Plateau Meteorology*, *32*(4), 1115–1125. https://doi.org/10.7522/j.issn.1000-0534.2012.00105
Zhang, Q., Li, J., Singh, V. P., Xu, C. Y., & Bai, Y. (2012). Changing structure of the precipitation process during 1960–2005 in Xinjiang, China. *Theoretical and Applied Climatology*, *110*(1), 229–244. https://doi.org/10.1007/s00704-012-0611-4
Zhang, C., & Ling, J. (2012). Potential vorticity of the Madden–Julian Oscillation. *Journal of the Atmospheric Sciences*, *69*, 65–78. https://doi.org/10.1175/JAS-D-11-081.1

Zhang, S., & Zhu, C. (2011). Possible causes of circulation anomalies associated with subsequent snowstorms over the north of Xinjiang during winter 2009 [in Chinese]. *Chinese Journal of Atmospheric Sciences*, *35*(5), 833–846. https://doi.org/10.3878/j.issn.1006-9895.2011.05.04

Zhao, T., & Dai, A. (2015). The magnitude and causes of global drought changes in the twenty-first century under a low–moderate emissions scenario. *Journal of Climate*, *28*(11), 4490–4512. https://doi.org/10.1175/JCLI-D-14-00363.1

Zhao, C., Yao, S., Ding, Y., & Wang, J. (2015). Detection of precipitation variability based on entropy over nearly 50 years in Xinjiang, northwestern China. *Theoretical and Applied Climatology*, *122*(3), 609–618. https://doi.org/10.1007/s00704-014-1318-5